Pressure-induced deactivation of core-shell nanomaterials for catalyst-assisted chemical looping

Jiawei Hu[a], Vladimir V. Galvita[a,*], Hilde Poelman[a], Christophe Detavernier[b], Guy B. Marin[a]

[a] Laboratory for Chemical Technology, Ghent University, Technologiepark 125, B-9052 Ghent, Belgium
[b] Department of Solid State Sciences, Ghent University, Krijgslaan 281, S1, B-9000 Ghent, Belgium

ARTICLE INFO

ABSTRACT

Catalyst-assisted chemical looping dry reforming is a promising technology for CO-rich syngas production with maximized CO_2 utilization, especially when performed auto-thermally, over core-shell nanomaterials in a double-zone reactor bed with first a Fe/Zr@Zr-Ni@Zr bifunctional catalyst and next a Fe/Zr@Zr oxygen storage material. Understanding the origin of the material deactivation under high-pressure conditions is essential to advance this technology towards industrial application. Therefore, pressure-induced material deactivation was studied through a series of on-site assessments (steady-state CH_4 reforming and prolonged redox cycling at 750 °C and 1–10 bar) and ex-situ characterization (STEM-EDX, XRD and N_2 adsorption-desorption).

At high pressure, both Fe/Zr@Zr-Ni@Zr and Fe/Zr@Zr show reaction-related deactivation, the origin of which can be ascribed to carbon deposition and particle sintering, respectively. During regular catalyst-assisted dry reforming over Fe/Zr@Zr-Ni@Zr, the rise of pressure decreases CH_4 conversion and increases carbon deposition on the Ni surface. Rapidly growing carbon filaments destroy the core-shell structure, resulting in segregation of the Ni-based particles from the catalyst bulk with concomitant severe sintering. During H_2/CO_2 redox cycling of Fe/Zr@Zr, an increased pressure decreases the time-averaged space-time yield of CO. In the reduction half-cycle, high pressure prolongs the existence of the FeO intermediate phase in the transformation of Fe/Zr@Zr, which decreases the material's melting point, leading to fast sintering. Adding a small amount of O_2 makes the chemical looping dry reforming process auto-thermal, which is advantageous in eliminating carbon. Nevertheless, deactivation of the double-zone reactor bed still occurs and is mainly ascribed to particle sintering, following similar principles as mentioned above.

For both regular and auto-thermal catalyst-assisted chemical looping dry reforming, the decreasing ability for CO_2 utilization is naturally due to the deactivation of the oxygen storage material, but also controlled by the stability of the bifunctional catalyst. The latter determines the reduction capacity of the gas product mixture in the reduction half-cycle, thereby affecting the achievable reduction degree of the oxygen storage material.

1. Introduction

To bolster the rapid economic growth of modern society, the entire world is facing increasing energy demands. Up to 2040, almost 80% of global energy supply still depends on fossil fuels, including coal, petroleum and natural gas [1,2]. However, fossil fuel-based energy production is widely considered as a leading cause for greenhouse gas emission such as CO_2, which is the largest contributor towards the global warming effect [3–7]. As the Intergovernmental Panel on Climate Control suggested, a 50–85% reduction in total CO_2 emission by 2050 is necessary to limit the anticipated global temperature increase to 2 °C [8].

Many efforts have been made in the past decades to develop innovative energy conversion technologies that not only satisfy economic benefits but also lower the environmental impact. Dry reforming of methane (DRM, Eq. (1)), a high value-added energy conversion technology, simultaneously converts two main greenhouse gases (CH_4 and CO_2) to syngas, a mixture of H_2 and CO, which is a crucial intermediate precursor in chemical industry [9,10].

$$CH_4 + CO_2 \leftrightarrows 2\,CO + 2H_2 \quad \Delta H_{298} = 247\,kJ \cdot mol^{-1} \tag{1}$$
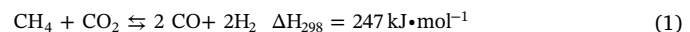
The capacity of CO_2 conversion can be further enhanced if DRM is implemented in a chemical looping process, i.e. chemical looping CH_4 dry reforming (CLDR). Bridged by the cyclic transformation of an oxygen storage material (OSM), generally a metal oxide (e.g. Fe_3O_4), this process is divided into two, spatially or temporally separated half-

---

cycles [11–16]: during the reduction half-cycle, the OSM is reduced by CH_4 and produces CO_2 and H_2O (Eq. (2)); During the subsequent re-oxidation half-cycle, CO_2 serves as an oxidizing agent to regenerate the OSM, simultaneously producing CO (Eq. (3)). Theoretically, CLDR (Eq. (4)) allows for a three times higher CO_2 conversion than conventional DRM (Eq. (1)) [17].

$$CH_4 + Fe_3O_4 \leftrightarrows 3\,Fe + CO_2 + 2H_2O \quad \Delta H_{298} = 315\,kJ \bullet mol^{-1} \qquad (2)$$

$$4CO_2 + 3\,Fe \leftrightarrows Fe_3O_4 + 4CO \quad \Delta H_{298} = 11.4\,kJ \bullet mol^{-1} \qquad (3)$$
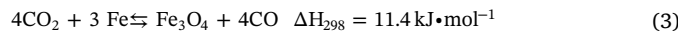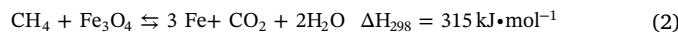
By summing up Eqs. (2) and (3), the overall reaction of CLDR, which is the endothermic CO_2 reforming of CH_4 into CO, can be obtained:

$$CH_4 + 3CO_2 \leftrightarrows 4\,CO + 2H_2O \quad \Delta H_{298} = 330\,kJ \bullet mol^{-1} \qquad (4)$$
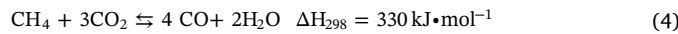
Different from DRM, aiming to high syngas yield, the goal of CLDR is now to enhance CO_2 utilization, thus CO becomes the main product. Afterwards, the immediate valorization of CO can be achieved by blending with renewable H_2, produced by the electrolysis of H_2O using renewable energy such as solar, wind or hydro, to form syngas with any desired H_2/CO ratio [10,18,19]. The adjustability of the H_2/CO ratio of syngas is of important for its flexible application in the synthesis of various industrial products, such as fuels, olefins and chemicals [20,21]. A recent study revealed that the valorization of CO_2 with CH_4 by CO production (e.g. via CLDR) followed by the conversion of CO with renewable H_2 into value-added product is an economically viable approach for carbon recycling, through which almost 50% of stationary CO_2 emissions from large point sources (such as industrial flue gases) could be converted into fuels, if only mass balances and market volumes are considered [22].

The CO_2 conversion in CLDR is limited by the slower step, which is the reduction of OSM by CH_4, especially in the presence of CO_2. The natural mixture of CH_4 and CO_2 significantly decreases the rate and degree of OSM reduction because CO_2 is an oxidant. Both CO_2 in the feed (when using biogas as fuel) and as a product have this retarding effect on the OSM reduction. In order to overcome this limitation, a novel process, so-called catalyst-assisted chemical looping CH_4 dry reforming (CCDR), is proposed. It is implemented over a bifunctional reactor bed composed of either a physical mixture of a reforming catalyst and an OSM, or a bifunctional material [17,23,24]. In CCDR, the mixture of CH_4 and CO_2 is pre-converted into syngas over the catalyst during the reduction half-cycle, so that the OSM can be fully reduced in the stream of and H_2 and CO, as both these gases have a considerably higher reducing activity than CH_4. Accordingly, a high CO_2 conversion can be reached upon OSM regeneration during the re-oxidation half-cycle. But the overall reaction (Eq. (4)) shows that the CCDR is a strongly endothermic process, entailing high energy consumption for reactor heating. This problem can be countered by co-feeding a small amount of O_2 with CH_4 and CO_2 during the reduction half-cycle, thus making the process auto-thermal [25–27]. Here, the CCDR is adjusted to yield an intensified process, i.e. catalyst-assisted chemical looping auto-thermal dry reforming (CCAR, Eq. (5)). Based on our previous study [28], the CCAR process can run in thermoneutral condition, i.e. $\Delta H = 0\,kJ\,mol^{-1}$, with a molar ratio of $CH_4:CO_2:O_2 = 1:2.4:0.3$ at 600 °C or with a molar ratio of $CH_4:CO_2:O_2 = 1:2:0.5$ at 750 °C.

$$CH_4 + xCO_2 + \frac{(3-x)}{2}O_2 \leftrightarrows (1 + x)\,CO + 2H_2O \quad \Delta H_{298} = 0\,kJ \bullet mol^{-1}$$
$$(5)$$
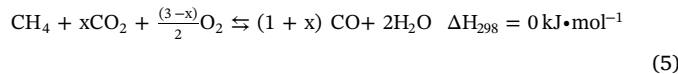
At the heart of all chemical looping technologies is the performance of the employed materials, which determines the process efficiency and sustainability. Much research pursues enhanced activity and stability of both reforming catalyst and oxygen storage material, the main approaches focusing on compositional and structural optimization [29,30], as in spinel [31,32], perovskite [33,34] and core-shell [35–38]. In our previous work [39], a core-shell Ni-Fe bifunctional nanomaterial (Fe/Zr@Zr-Ni@Zr), constructed from a ZrO_2-coated

Fe_2O_3/ZrO_2 core (Fe/Zr@Zr) and a ZrO_2-coated Ni shell (Ni@Zr), was designed to provide two functions, catalyst and oxygen storage, by the Ni-based shell and the Fe-based core, respectively. It showed superior catalytic activity and good redox stability during prolonged catalyst-assisted chemical looping without significant carbon deposition and particle sintering. Careful spatial distribution of Ni and Fe in a double-zone fixed-bed configuration, with Fe/Zr@Zr-Ni@Zr (as bifunctional catalyst) in a first zone and Fe/Zr@Zr (as OSM) in the second, further enhanced the capacity for CO_2 utilization.

In industrial applications, a chemical looping sector usually needs to be operated at high pressure (20–35 bar), in order to maintain a high circulation efficiency in the entire process [40–42]. However, high-pressure operation leads to a more harsh environment, which will result in deactivation of the employed catalysts and OSMs. According to thermodynamics [43], the carbon formation increases with pressure in CH_4 dry reforming, which was equally confirmed by pressurized dry reforming experiment [44]. The carbon deposition is considered the most important reason for the fast deactivation of the catalyst, especially Ni-based materials [45,46]. Tomishige et al. [47] investigated the activity and carbon deposition behavior of a NiO-MgO solid solution catalyst in pressurized CH_4 dry reforming. They found that the deposition of carbon on Ni particles is inevitable under high pressure, but a catalyst with low surface area shows a lower carbon formation rate. Hence, this rate will decrease with the aggregation of Ni particles, progressing in pressurized conditions. Otsuka et al. [48,49] reported that the carbon deposition during CH_4 decomposition can further promote the sintering of Ni particles to form larger clusters. In addition, the redox properties of the OSM are also significantly affected by pressure. García-Labiano et al. [50] investigated the redox kinetics of Al_2O_3 supported Cu, Ni and Fe OSMs using a pressurized thermogravimetric analysis, observing a negative correlation between pressure and the redox reaction rates for all studied materials, which was probably caused by an internal restructuring of the Al_2O_3 support. The analysis by Hammers et al. [51] supported these findings in that the increase of pressure has a negative impact on the reactivity of the OSM, which is kinetically controlled. In a recent study [41], the difference in gas-solid-phase redox reaction kinetics between high pressure (10 bar) and atmospheric pressure (1 bar) was monitored by an experimental study of pressurized chemical looping combustion of CH_4 and syngas using Cu- and Ni-based OSMs. The results show that high-pressure operation not only increases the carbon deposition over both OSMs but also decreases their reduction degree and oxidation kinetics.

Undoubtedly, pressure is a very important factor for the design, scale-up and optimization of a chemical looping technology, and understanding the effect of pressure on the material performance as well as the origin of material deactivation is therefore crucial. As a further development of our previous work, i.e. the double-zone fixed-bed reactor, with the Fe/Zr@Zr-Ni@Zr bifunctional catalyst, followed by Fe/Zr@Zr providing the main redox activity, as optimal configuration for the CCAR process, we now looked into the effect of pressure on this configuration. First, the materials from the two zones are evaluated separately: the Fe/Zr@Zr-Ni@Zr catalyst during CH_4 dry reforming and Fe/Zr@Zr during H_2/CO_2 redox cycling, at 1 bar and 10 bar. The deactivation origin for both core-shell structured nanomaterials at high pressure is discussed, with focus on carbon deposition and particle sintering. Eventually, the effect of pressure on the CO_2 utilization capacity of the complete double-zone reactor bed and its dependency on material deactivation, during catalyst-assisted chemical looping auto-thermal dry reforming was assessed.

2. Experimental

2.1. Materials preparation

A combination of impregnation and nanocoating was used to synthesize the core-shell structured Fe/Zr@Zr OSM. The latter then served

as core for synthesis of the core-shell structured Fe/Zr@Zr-Ni@Zr bi-functional catalyst, during which a SiO_2 template-assisted etching method was introduced to create a hollow nanostructure. The entire synthesis route was monitored through the evolution of the morphological structure of the synthesized products confirmed by STEM-EDX element mapping (Fig. S1, Supplementary Information). Details of the entire synthesis procedure can be found in our previous work [39].

2.2. General characterization

ICP-AES was applied to find the actual chemical composition of as-prepared materials after mineralization by peroxide fusion (ICAP 6500, Thermo Scientific). The specific surface area followed from the five point method of Brunauer-Emmett-Teller (BET; Micromeritics Tristar). Average pore size and pore volume were determined by N_2 adsorption-desorption at $-196\,°C$ using the Barrett-Joyner-Halenda method (Gemini Micromeritics). Ex-situ X-ray diffraction (XRD) measurements provided the crystallographic phases of the fresh and spent samples (Siemens Diffractometer Kristalloflex D5000, with Cu Kα radiation; 2θ range: 10° to 80°, step of 0.02°, counting time: 30 s/angle.). The crystallite size was determined from the peak width through the Scherrer equation [52].

Conventional transmission electron microscopy (TEM), scanning transmission bright field (STEM BF) and energy dispersive X-ray analysis (EDX) were carried out to retrieve morphological, structural and local chemical analyses (JEOL JEM-2200FS Cs-corrected microscope, operated at 200 kV, with a Schottky-type field emission gun (FEG) and EDX JEOL JED-2300D). (S)TEM samples were prepared by immersion of a lacey carbon film on a copper grid into the material powder and blowing off of the excess powder. Secondary X-ray fluorescence in EDX spectra was eliminated by a Be specimen retainer.

Time-resolved in-situ XRD measurements in θ-2θ mode (Bruker-AXS D8 Discover, Cu Kα radiation, linear detector 20° range, angular resolution of ˜0.1°, pattern collection time: 10 s) were applied to follow the evolution of crystallographic materials changes during reaction [28,39]. H_2/CO_2 redox cycling was carried out at 750 °C with alternating H_2 reduction and CO_2 re-oxidation sequences, after heating the samples to the targeted temperature at a rate of 60 °C·min^{-1} in He. Each cycle (8 min in total) consisted of 2 min material reduction (with 5% H_2/He), 2 min material re-oxidation (with pure CO_2) and 2 min intermediate He purging. Additionally, chemical looping dry reforming of CH_4 was performed at 750 °C with alternating CH_4 dry reforming and material regeneration sequences using CO_2. Prior to the dry reforming reaction, the sample was reduced in a flow of 5% H_2/He up to 750 °C at a rate of 20 °C·min^{-1} to reach the active state. After 2 min He purging, the reactant feed was switched to the reactor chamber. Each cycle (11 min) consisted of 5 min CH_4 dry reforming (with a molar ratio of CH_4:CO_2:He = 1:1:1), 2 min material regeneration (with pure CO_2) and 2 min intermediate He purging. In these measurements, the flow rates of all gas feeds were 60 NmL·min^{-1}.

2.3. Reactor setup and procedures

Activity and stability tests were performed in a tubular microreactor (i.d. 9 mm and length 460 mm) housed inside an electric furnace. A quartz reactor was used for the experiments at atmospheric pressure while an amorphous silicon-coated incoloy alloy 800 H T reactor was used for the high-pressure experiments. A bed of 100 mg of sample, homogeneously diluted with α-Al_2O_3 in a 1:20 mass ratio, was packed between quartz wool plugs. K-type thermocouples touching the outside and inside of the reactor at the position of the sample bed allowed measuring the sample temperature. Calibrated Bronkhorst mass flow controllers maintained the inlet gas flow rates, while the outlet gas stream was monitored online using an OmniStar Pfeiffer mass spectrometer (MS). The latter was calibrated beforehand for different mixtures of reactants and products and its response was regularly verified.

H_2 was followed at 2, He at 4, CH_4 at 16, H_2O at 18, CO at 28, O_2 at 32, Ar at 40 and CO_2 at 44 AMU. Concentrations were assessed taking into account the fragmentation patterns of the compounds, and contributions from unavoidable interference with fragmentation peaks of other gases were removed by adequate correction.

The catalytic activity and stability of the Fe/Zr@Zr-Ni@Zr bifunctional catalyst under different pressures at a constant temperature of 750 °C was evaluated in steady-state CH_4 reforming for 10 h time-on-stream (TOS). The reactor bed configuration is shown in Fig. S2a. Three steady-state experiments were performed: dry reforming of CH_4 (feed: a mixture of CH_4 + CO_2 + Ar with molar ratio of 1: 1: 0.4, Ar as internal standard) at 1 bar and at 10 bar, as well as auto-thermal dry reforming of CH_4 (feed: a mixture of CH_4 + CO_2 + O_2 + Ar with molar ratio of 1: 1: 0.1: 0.3) at 10 bar. Prior to the reforming reactions, the sample was reduced in a 200 NmL·min^{-1} flow of 10% H_2/Ar from room temperature to 750 °C (ramp rate: 10 °C·min^{-1}) at atmospheric pressure to reach the active state. After a 10 min purging step in Ar (for 10 bar experiments, the reactor was pressurized to the targeted pressure during this purging), the mixture feed with a total flow rate of 200 NmL·min^{-1} was allowed into the reactor. After 10 h, the reactor system was again purged with Ar for 10 min (for 10 bar experiments, the pressure was decreased to atmospheric pressure during purging), and subsequently the sample was regenerated: first, the removal of deposited carbon by complete oxidation with 10% O_2/He (200 NmL·min^{-1}) took place, followed by reduction of the sample in 10% H_2/Ar for 10 min. Finally, the activity of the regenerated sample was evaluated by means of a steady-state reforming reaction for 30 min.

The redox activity and stability of the Fe/Zr@Zr OSM at 1 and 10 bar was assessed by prolonged H_2/CO_2 redox cycling (20 cycles, 6 h in total) at 750 °C. The reactor bed configuration is depicted in Fig. S2b. In order to avoid carbon formation affecting the evaluation of the actual oxygen storage capacity of the OSM, H_2 was used as reducing gas in the reduction half-cycle. Each cycle (18 min in total) comprised 4 min material reduction and 4 min material re-oxidation, separated by 5 min intermediate Ar purging. 20% H_2/Ar (Ar is an internal standard), 20% CO_2/Ar and pure Ar were used as reducing, oxidizing and purging gas, respectively. All gas flow rates were 200 NmL·min^{-1}. Before the redox cycling started, the sample bed was heated and pressurized to the targeted temperature and pressure under Ar.

The behavior of the double-zone reactor bed with Fe/Zr@Zr-Ni@Zr bifunctional catalyst and Fe/Zr@Zr OSM (Fig. S2c) during catalyst-assisted chemical looping auto-thermal dry reforming (CCAR) at different pressures was examined with repeated cycles at 750 °C. Prior to the CCAR experiment, the samples were reduced in 10% H_2/Ar (200 NmL·min^{-1}) from room temperature to 750 °C (with a heating ramp of 10 °C·min^{-1}) at atmospheric pressure as activation procedure. After the reactor was stabilized at the targeted pressure (in Ar), 20 cycles of CCAR were carried out with alternating 2 min reduction and 2 min re-oxidation sequences (always with 7 min of Ar purging in between) at a constant flow rate of 200 NmL·min^{-1}. The reducing feed was a mixture of CH_4:CO_2:O_2:Ar (at a molar ratio of 1:1:0.1:0.3) and the oxidizing feed was 20% CO_2/Ar.

In order to identify the origin of sintering of the Fe/Zr@Zr OSM and the Fe/Zr@Zr-Ni@Zr bifunctional catalyst under pressurized conditions, the changes in the structure of spent samples collected from a blank experiment (Ar treatment experiment), i.e. keeping the samples at 750 °C and 10 bar in an Ar stream (200 NmL·min^{-1}) for 10 h, were characterized.

The following expressions are used to determine the activity of the bifunctional catalyst and OSM in the different reactor bed configurations. The percent conversion for a reactant is calculated as:

$$X_i = \frac{F_{0,i} - F_i}{F_{0,i}} \times 100\% \tag{6}$$

where $F_{0,i}$ and F_i (mol·s^{-1}) are the inlet and outlet molar flow rates of

reactant i.

The space-time yield (STY, $mol \cdot s^{-1} \cdot kg_M^{-1}$) is calculated from the difference between the inlet and outlet molar flow rates:

$$STY_i = \frac{|F_{0,i} - F_i|}{W_M} \tag{7}$$

where $F_{0,i}$ and F_i ($mol \cdot s^{-1}$) are the inlet and outlet molar flow rates of component i, and W_M (kg_M) is the mass of material in the reactor, i.e. W_{Ni} and W_{Fe2O3} to calculate STY in CH_4 dry reforming and in redox cycling, respectively.

In addition, the amount of carbon formed, during the reduction half-cycle of the CCAR process, is determined by the carbon balance between the inlet and outlet products :

$$CH_{4in} + CO_{2in} = CH_{4out} + CO_{2out} + CO_{formed} + C_{formed} \tag{8}$$
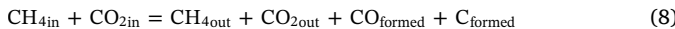
where CH_{4in} (or CH_{4out}) and CO_{2in} (or CO_{2out}) ($mol \cdot kg_{Ni}^{-1}$) are the inlet (or outlet) amounts of CH_4 and CO_2, the CO_{formed} and C_{formed} ($mol \cdot kg_{Ni}^{-1}$) are the amounts of the formed CO and carbon.

In order to compare CO_2 utilization during chemical looping in steady-state operation, a dynamic simulation for a multi-tubular reactor configuration was performed based on the experimental CO space-time yield of the single-tubular reactor. A multi-tubular reactor configuration resembles the multi-column configuration in a pressure-swing adsorption (PSA) process, where each column is cycled between adsorption and regeneration and allows continuous processing of a given feed stream. The core of the simulation concept for such a multi-tubular reactor is that all single-tubular reactors are operated in chemical looping regime, but sequentially, i.e. with a delay relative to the preceding one (Fig. S3a). In this way, a redox cycle is established in each single-tubular reactor by switching the feed valves at discrete times, leading to an overall oscillating CO space-time yield with constant amplitude, a so-called permanent periodic regime. The oscillatory space-time yield (STY_{osc}, $mol_{CO} \cdot s^{-1} \cdot kg_{Fe2O3}^{-1}$) is defined by Eq. (9). It is determined by summing the contributions of all reactors (based on the single-tubular reactor experiment) at each time step and subsequent division by the number of reactors that are in material oxidation mode, n_{ox}, in order to take into account the utilization of a higher amount of active material.

$$STY_{osc} = \frac{\sum_{n_{ox}} F_{CO}}{n_{ox} * W_{Fe2O3}} = \frac{\sum_{n_{ox}} STY_{CO}}{n_{ox}} \tag{9}$$

where F_{CO} ($mol_{CO} \cdot s^{-1}$) is the outlet molar flow rate of CO product and W_{Fe2O3} (kg_{Fe2O3}) is the mass of Fe_2O_3 in the reactor. This value is used for calculating the $\overline{STY}_{CO}$ ($mol_{CO} \cdot s^{-1} \cdot kg_{Fe2O3}^{-1}$), which is the average value of the STY_{osc} in the permanent periodic regime. An example of the calculation process of the $\overline{STY}_{CO}$ is shown in Fig. S3b.

2.4. Thermodynamic analysis

For analysis of the thermodynamic behavior of a given process, the EkviCalc software package [53] was used, which contains a large thermodynamic database of solid, liquid and gas phase species, as well as possible reaction pathways between these species. Hence, given an initial amount of reactant species, thermodynamic equilibrium at a specified temperature and pressure can be calculated. This is done by minimizing the Gibbs free energy $G_{P,T}$ of the system at these given conditions:

$$dG_{P,T} = \sum_{i=1}^{m} \mu_i dn_i = 0 \tag{10}$$

where m is the number of reactant and product species, μ_i ($J \cdot mol^{-1}$) is the chemical potential of species i at pressure P (bar) and temperature T (°C), n_i (mol) is the amount of species i, and $G_{P,T}$ (J) is the Gibbs free energy of the system at pressure P and temperature T.

In the present investigations, following analyses were performed:

(1) thermodynamic analysis on auto-thermal dry reforming of CH_4 at atmospheric pressure over a broad range of temperatures (from 200 to 1000 °C) or at fixed temperature (750 °C) over a wide range of pressures (from 1 to 20 bar). The given initial moles of reactant gases are 10 mol CH_4 + 10 mol CO_2 + 1 mol O_2 + 3 mol Ar. With the stepwise variation of temperature or pressure, the equilibrium product composition (mole fraction of CH_4, CO_2, O_2, H_2, CO, H_2O and C) was determined;

(2) thermodynamic calculations concerning the iron oxide reducibility under $(H_2 + CO)/(H_2O + CO_2)$ were carried out at 1 bar or 10 bar over a range of temperatures from 200 to 1000 °C. The starting point is 1 mol of Fe_2O_3 and 10 mol of gas. Using a constant ratio of C and H (1:2 M ratio), the gas phase composition (mole fraction of H_2, H_2O, CO and CO_2) is varied stepwise and the phase diagram of iron can be constructed.

3. Results and discussion

3.1. Material characterization

The morphology of the as-prepared core-shell structured Fe/Zr@Zr (OSM) and Fe/Zr@Zr-Ni@Zr (bifunctional catalyst) has been presented in previous work [39]. The OSM serves as starting point for the bifunctional catalyst and the different synthesis steps are illustrated in Fig. S1.

The general properties, such as BET specific surface area, average pore size and pore volume, actual metal content and crystallite size of the main crystalline phases, of the as-prepared core-shell structured Fe/Zr@Zr and Fe/Zr@Zr-Ni@Zr are reported in Table S1. As reported in previous work [37], ZrO_2 support in the core is monoclinic (m-), while tetragonal ZrO_2 (t-) dominates the shell. The m-ZrO_2 crystallites show similar size in both materials, due to the fact that they originate from the same core — Fe_2O_3/ZrO_2. However, the t-ZrO_2 crystallite size of Fe/Zr@Zr-Ni@Zr is smaller than the one of Fe/Zr@Zr, indicating a smaller particle size in the outer shell of Fe/Zr@Zr-Ni@Zr. This could contribute to its larger specific surface area and smaller pore size. Because the crystallite size of Ni species in Fe/Zr@Zr-Ni@Zr is smaller than the XRD detection limit (~ 3 nm), the Ni-related phase in the as-prepared bifunctional catalyst cannot be observed in the XRD pattern, but it has been identified by XPS measurements, showing co-existing NiO and Ni_2O_3 phases, as described in previous work [39].

The redox behavior of Fe/Zr@Zr and Fe/Zr@Zr-Ni@Zr in a chemical looping process was determined by the evolution of their crystal phases during H_2/CO_2 redox cycling at 750 °C, monitored by in-situ XRD. Characteristic peaks associated with crystalline ZrO_2 (the unlabeled diffraction peaks in the 2D XRD patterns) in both materials remain visible throughout the whole in-situ measurement without any shift, indicating neither reduction nor oxidation of ZrO_2 occurs under the present experimental conditions. For Fe/Zr@Zr (Fig. 1a), the evolution of the iron-related phase follows the consecutive transitions $Fe_3O_4 \rightarrow FeO \rightarrow Fe$ during the reduction half-cycle, while metallic Fe is directly oxidized to Fe_3O_4 by CO_2 in the re-oxidation half-cycle. For Fe/Zr@Zr-Ni@Zr (Fig. 1b), the transformation of the iron-related phase during redox cycling approximately follows the same steps as Fe/Zr@Zr. However, a diffraction of Ni-Fe alloy appears simultaneously with the formation of metallic Fe during the reduction half-cycle, and disappears in the re-oxidation half-cycle, due to the decomposition of the alloy to Ni and Fe_3O_4 by CO_2. These observations are confirmed by comparing the XRD peaks in the 2θ range of 42.5° ~ 45.5° in the redox cycling of Fe/Zr@Zr and Fe/Zr@Zr-Ni@Zr (Fig. S4a–b). Although Fe_3O_4 can be regenerated from the Ni-Fe alloy, the alloy formation does favor particle sintering, accordingly reducing the oxidation rate of the alloyed Fe species [17,39]. Additionally, the Fe_2O_3 content of the bifunctional catalyst is limited (Table S1), so the oxygen storage capacity for CO_2 utilization of the proposed double-zone reactor bed (Fig. S2c) is ensured mostly by the Fe/Zr@Zr OSM in the second zone.
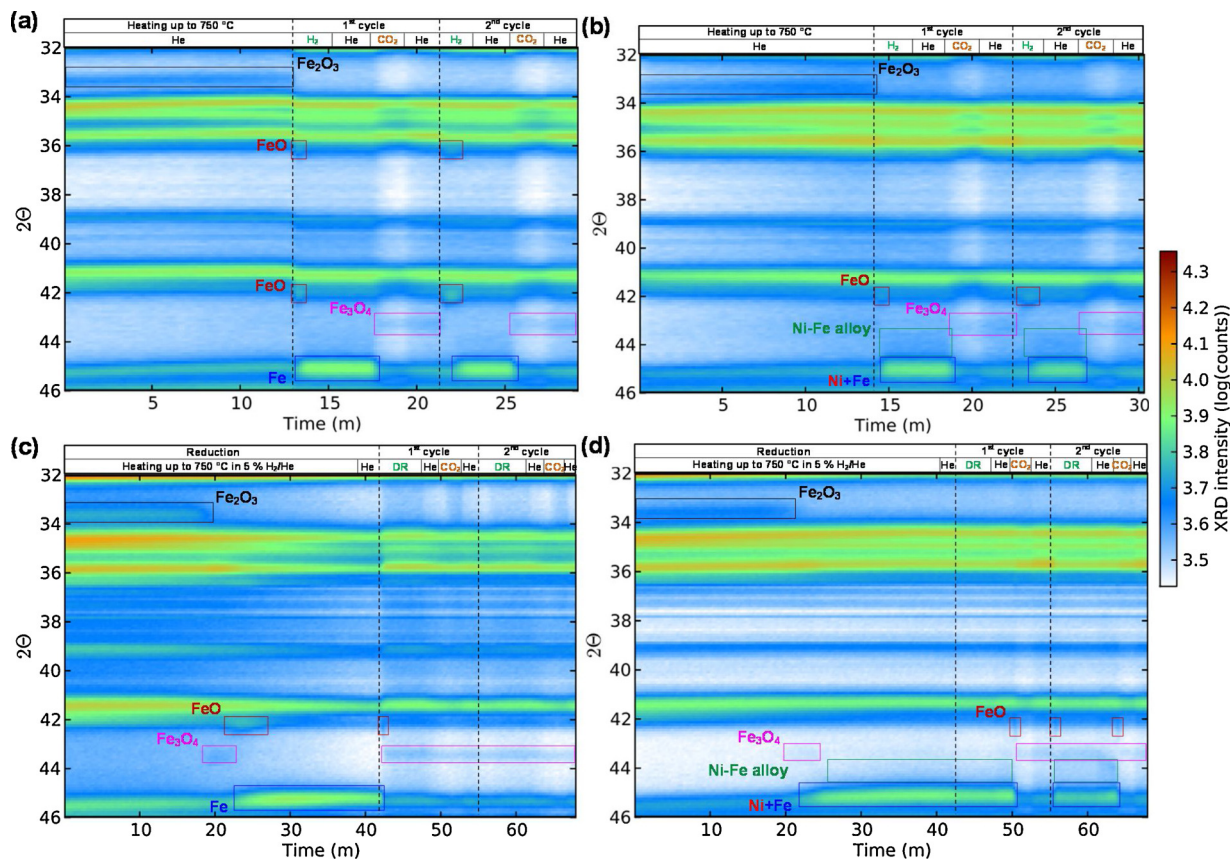
Fig. 1. 2D in-situ XRD patterns recorded: (a, b) during H_2/CO_2 redox cycling at 750 °C and 1 bar for Fe/Zr@Zr OSM (a) and Fe/Zr@Zr-Ni@Zr bifunctional catalyst (b). Each cycle (8 min) comprises 2 min material reduction by H_2 (gas: 5% H_2/He), 2 min material re-oxidation by CO_2 (gas: pure CO_2) and 2 min intermediate He purging; (c, d) during chemical looping dry reforming of methane at 750 °C and 1 bar for Fe/Zr@Zr OSM (c) and Fe/Zr@Zr-Ni@Zr bifunctional catalyst (d). Each cycle (11 min) comprises 5 min methane dry reforming (DR) (gas: mixture of CH_4:CO_2:He = 1:1:1), 2 min material regeneration by CO_2 (gas: pure CO_2) and 2 min intermediate He purging. All gas flow rates were 60 NmL·min^{-1}.

The reactivity of Fe/Zr@Zr and Fe/Zr@Zr-Ni@Zr in chemical looping methane dry reforming at 750 °C was equally monitored by in-situ XRD (Fig. 1c–d). Prior to dry reforming of CH_4, the materials were reduced by H_2-TPR to 750 °C, in order to form metallic Fe in Fe/Zr@Zr and co-existing metallic Fe and Ni with Ni-Fe alloy in Fe/Zr@Zr-Ni@Zr. Then, a mixture of CH_4 and CO_2 (at a molar ratio of 1:1) was introduced to the reactor chamber for 5 min dry reforming, followed by 2 min re-oxidation of materials with CO_2. For Fe/Zr@Zr (Fig. 1c), metallic Fe is rapidly transformed into Fe_3O_4 after contact with the CH_4 and CO_2 mixture, where after the Fe_3O_4 peak remains almost constant (as seen in Fig. S4c). This fast oxidation of metallic Fe indicates that there is insufficient syngas generated from CH_4 dry reforming (Eq. (1)), hence the metallic Fe is oxidized to Fe_3O_4 under the dominant presence of oxidizing gas (CO_2) over reducing gases (CO and H_2). The latter also indicates that CH_4 dry reforming cannot be activated over metallic Fe. For Fe/Zr@Zr-Ni@Zr (Fig. 1d), all metallic phases remain constant during dry reforming in the first cycle and Fe_3O_4 does not appear until the feeding gas is switched to pure CO_2 (as equally illustrated in Fig. S4d), implying that a considerable amount of reducing gases is produced over the bifunctional catalyst during CH_4 dry reforming. In the second cycle, the metallic Fe, Ni and Ni-Fe alloy peaks quickly reappear when feeding the CH_4 and CO_2 mixture, indicating its conversion into CO and H_2 has resumed, both of which reduce Fe_3O_4. The above discussion exemplifies the importance of the addition of Ni for catalyzing CH_4 dry reforming. Therefore, the activity for catalyzing CH_4 dry reforming over the double-zone bed (Fig. S2c) is provided by the Fe/Zr@Zr-Ni@Zr bifunctional catalyst in the first zone.

3.2. Effect of pressure

3.2.1. The behavior of the bifunctional catalyst

The effect of operating pressure on the activity and stability of the Fe/Zr@Zr-Ni@Zr bifunctional catalyst was assessed in steady-state CH_4 reforming at 750 °C, 1 bar and 10 bar. As shown in Fig. 2, the initial CH_4 conversion during dry reforming at 10 bar (process labeled as DR10) is lower than the one during dry reforming at 1 bar (DR1), in line with the equilibrium values. Owing to the endothermicity of the dry reforming reaction, an increase in operating temperature is required to achieve high CH_4 conversion at high pressure [54]. Further, the CH_4 conversion decreases with time-on-stream (TOS) in both DR1 and DR10, indicating deactivation of the bifunctional catalyst during dry reforming. In DR1, the activity of the catalyst only shows a slight decrease (10% loss of CH_4 conversion) after 10 h, while it decreases faster and to a larger extent in DR10 (87% loss).

Both carbon deposition and sintering are known to be main causes for deactivation of Ni-based catalysts under conditions of CH_4 dry reforming [55,56]. Hence, the carbon deposited on the bifunctional catalyst was determined as the CO_2 yield upon O_2 oxidation of the spent samples. The CO_2 produced by the spent sample from DR10 (spent_DR10, total CO_2 yield = 7023 mol·kg_{Ni}^{-1}) is about 7 times as much as by the spent sample from DR1 (spent_DR1, total CO_2 yield = 1049 mol·kg_{Ni}^{-1}). This indicates that the increase of pressure aggravates carbon deposition, thereby resulting in more severe deactivation. After regeneration, neither sample could restore the initial activity completely (Fig. 2), probably due to the irreversible deactivation caused by particle sintering. The fact that the activity of spent_DR10 is less restored than the one of spent_DR1 (46% vs. 95% of the initial
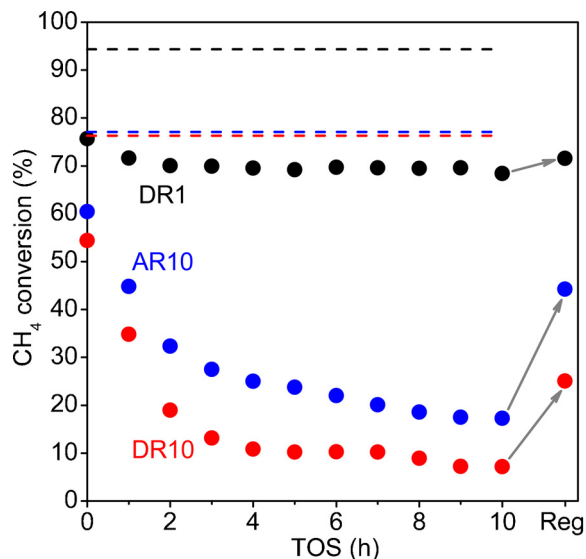
Fig. 2. CH$_4$ conversion over the Fe/Zr@Zr-Ni@Zr bifunctional catalyst during 10 h dry reforming (feed: a mixture of CH$_4$:CO$_2$:Ar = 1:1:0.4) at 750 °C, 1 bar (●) and 10 bar (●), as well as 10 h auto-thermal dry reforming (feed: a mixture of CH$_4$:CO$_2$:O$_2$:Ar = 1:1:0.1:0.3) at 750 °C, 10 bar (●). The grey arrows point to the CH$_4$ conversion regained on the regenerated materials (Reg.); The dashed lines show the equilibrium values of CH$_4$ conversion in dry reforming (reactant: a mixture of CH$_4$:CO$_2$:Ar = 1:1:0.4) at 750 °C, 1 bar (black line) and 10 bar (red line), as well as in auto-thermal dry reforming (feed: a mixture of CH$_4$:CO$_2$:O$_2$:Ar = 1:1:0.1:0.3) at 750 °C, 10 bar (blue line).

value) suggests a more severe sintering of the bifunctional catalyst under high-pressure dry reforming.

Auto-thermal dry reforming process, i.e. reforming of a mixture of CH$_4$, CO$_2$ and O$_2$, combining dry and partial oxidative reforming of CH$_4$, has been reported to be effective in energy conversion and enhancement of catalyst stability [9]. As a next step in this study, a small amount of O$_2$ was co-fed with CH$_4$ and CO$_2$, expecting to mitigate the severe deactivation during CH$_4$ dry reforming at high pressure. Compared to DR10, the initial CH$_4$ conversion during auto-thermal dry reforming at 10 bar (process label AR10) is higher (Fig. 2), owing to the combined consumption of CH$_4$ through combustion (CH$_4$ + 2O$_2$ → CO$_2$ + 2H$_2$O) and partial oxidation (CH$_4$ + 0.5O$_2$ → CO + 2H$_2$), confirmed by the increase in both initial H$_2$O yield and H$_2$/CO molar ratio (Fig. S5). This means that high CH$_4$ conversion can be maintained at high pressure by adding oxygen to the feed. Upon oxidation treatment of the spent catalyst, the CO$_2$ production over the spent sample from AR10 (spent_AR10) (2007 mol·kg$_{Ni}^{-1}$) is less than 1/3 of that on spent_DR10 (7023 mol·kg$_{Ni}^{-1}$), demonstrating that the deposited carbon is significantly decreased during auto-thermal dry reforming of CH$_4$. This can be ascribed to the in-situ removal of carbon by the co-fed O$_2$. Moreover, the spent_AR10 can regain 73% of the initial activity after regeneration (Fig. 2), i.e. much more than spent_DR10, implying an obvious mitigation of catalyst sintering during auto-thermal dry reforming.

The effect of pressure on the deactivation of the Fe/Zr@Zr-Ni@Zr bifunctional catalyst was determined by characterization of the changes in morphology and crystalline structures. After 10 h of steady-state CH$_4$ reforming, spent_DR1 shows good stability of its eccentric core-shell structure (Fig. 3a), compared to the fresh sample (Fig. S1g): the Fe/Zr@Zr OSM core is still encapsulated by the outer Ni@Zr shell, and in the latter Ni is still well coated by ZrO$_2$. The particle size of Fe remains constant and the one of Ni only shows a slight increase owing to sintering. The vast majority of Ni particles remain smaller than 8 nm, only one large particle appears at the same spot as the Fe core, as a result of the formation of the Ni-Fe alloy during CH$_4$ dry reforming. The latter is confirmed by the XRD patterns of the spent samples (Fig. S6).

For spent_DR10 (Fig. 3b), the morphological structure of the catalyst is severely damaged: the core-shell structure has collapsed and is aggregated, most of Fe and Ni now form alloy, some alloy particles have migrated out of the bulk of the catalyst, and particles have suffered from severe sintering. In addition, it is worth noting that deposited carbon is observed on this sample, as seen in the inset of the STEM image in Fig. 3b. Filamentous carbon appears on the surface of the catalyst and wraps around large Ni-Fe alloy particles that are separated from the bulk of the catalyst. For spent_AR10 (Fig. 3c), in contrast, no obvious carbon is seen and the core-shell structure persists, while particle sintering is milder than on spent_DR10.

The changes in the crystallite size of the main crystal phases and the texture properties of the spent bifunctional catalysts are displayed in Fig. 4. For all spent samples, the crystallite size of m-ZrO$_2$ almost remains unchanged compared to the fresh sample (Fig. 4a), showing a good stability of the ZrO$_2$ support. For the sample which experienced a 10 h Ar treatment at 750 °C and 10 bar (process label Ar10), only a minor increase in the crystallite size of Fe$_2$O$_3$ and t-ZrO$_2$ is observed (Fig. 4a), and the Ni-related phase remains unobservable in the XRD pattern (Fig. S6b), indicating that pressurized operation does not contribute to particle sintering when no reaction occurs. This is further confirmed by comparison of the texture properties of this sample with the fresh one, in Fig. 4b: the small average pore size pertains and only slight decreases in the specific surface area and the average pore volume are noticed. After 10 h steady-state CH$_4$ reforming (DR1, DR10 and AR10), however, the spent catalysts show obvious increases in the crystallite size of Fe$_3$O$_4$, Ni$_3$Fe and t-ZrO$_2$ (Fig. 4a), evidencing the sintering of both the iron oxide core and the Ni@ZrO$_2$ shell. Such sintering, anyhow, results in the partial collapse and blockage of mesopores, thus leading to an increase of the average pore size, as well as a decrease in average pore volume and specific surface area (Fig. 4b). Additionally, the increase in crystallite size of the spent catalyst after DR10 is clearly larger than for the one after DR1, indicating a significant effect of the pressurized operation on particle sintering when reactions occur. This can be ascribed to the fact that, as shown above, the higher pressure aggravates carbon deposition on the Ni-Fe alloy surface during CH$_4$ dry reforming, weakening the stability of the core-shell structure of the bifunctional catalyst and accordingly leading to particle aggregation. However, the addition of O$_2$ to the reforming feed can eliminate carbon deposits via in-situ removal, which contributes to maintain the integrity of the core-shell structure, protecting the particles from aggregation. As Fig. 4a shows, the crystallite sizes of Fe$_3$O$_4$, Ni$_3$Fe and t-ZrO$_2$ in the spent catalyst after AR10 are significantly smaller than after DR10, showing the advantage of the auto-thermal dry reforming process in the mitigation of particle sintering at high pressure.

Based on the above discussion, the origin of the deactivation of the Fe/Zr@Zr-Ni@Zr bifunctional catalyst during high-pressure CH$_4$ dry reforming can be elaborated: when reactions occur over the catalyst, high pressure aggravates the carbon deposition. Carbon nucleates on the surface of the Ni-based (metallic Ni and Ni-Fe alloy) particles and rapidly grows into carbon filaments, which then wrap around these particles. The formation of carbon filaments and their spread over Ni particles during coking in CH$_4$ dry reforming are equally confirmed by a recent study [57]. Parallel to the continuous extension of the filaments, the encapsulated Ni-based particles are pushed out of the outer ZrO$_2$ shell, leading to collapse of the core-shell structure and segregation of the Ni-based particles from the catalyst. Without protection of the ZrO$_2$ shell, these have stronger tendency to form alloy and undergo sintering, while larger Ni particles are also more favorable to carbon deposition. Fast sintering of Ni-based catalysts in relation to carbon deposition under high-pressure CH$_4$ dry reforming was equally reported in literature [47]. The authors performed steady-state CH$_4$ dry reforming (CH$_4$:CO$_2$ = 1:1) over a Ni$_{0.1}$Mg$_{0.9}$O solid solution catalyst at 850 °C and 20 bar for 4 h, during which aggregation of Ni particles occurred rapidly at the very initial stage, accompanied by carbon formation, and
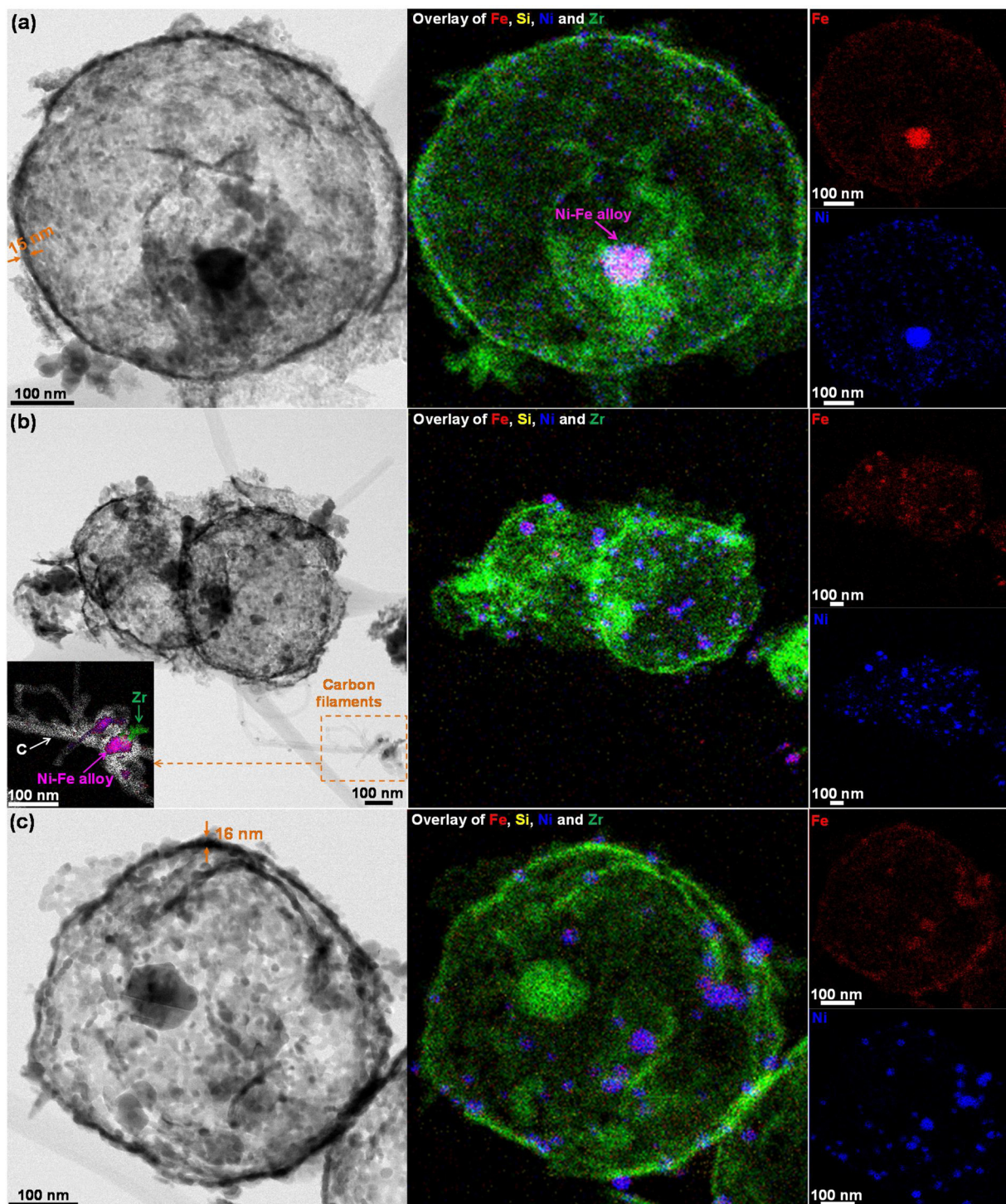
Fig. 3. STEM micrograph and EDX element mapping of Fe (red color), Si (yellow), Ni (blue) and Zr (green), and the overlay mapping of these elements for the samples of Fe/Zr@Zr-Ni@Zr bifunctional catalyst after 10 h dry reforming at 750 °C and (a) 1 bar (named as spent_DR1) or (b) 10 bar (spent_DR10), as well as (c) 10 h auto-thermal dry reforming at 750 °C and 10 bar (spent_AR10).

the amount of carbon increased linearly with time-on-stream.

3.2.2. The behavior of the oxygen storage material

The influence of operating pressure on the redox activity and stability of the Fe/Zr@Zr OSM was assessed by prolonged H_2/CO_2 redox cycling at 750 °C, under 1 bar and 10 bar. In each redox cycle, the iron oxide of the OSM is first reduced to metallic Fe by H_2 during the reduction half-cycle. After purging the reactor bed with Ar, CO_2 is fed to regenerate the OSM, i.e. re-oxidize metallic Fe to Fe_3O_4, simultaneously

producing CO during the re-oxidation half-cycle. Fig. 5a displays the space-time yield of CO in the first H_2/CO_2 redox cycle for different pressures. The total molar yields of CO (obtained by integration of the STY_{CO} peak) during 4 min re-oxidation at 1 bar and 10 bar are 16.5 $mol \cdot kg_{Fe2O3}^{-1}$ and 15.6 $mol \cdot kg_{Fe2O3}^{-1}$, respectively. Both values are similar to the achievable maximum yield value (~ 17 $mol \cdot kg_{Fe2O3}^{-1}$), i.e. the total oxygen storage capacity of the OSM from CO_2 calculated based on the equation: $3Fe + 4CO_2 \rightarrow Fe_3O_4 + 4CO$. This indicates that in this cycle the oxygen storage capacity of the Fe/Zr@Zr OSM can be
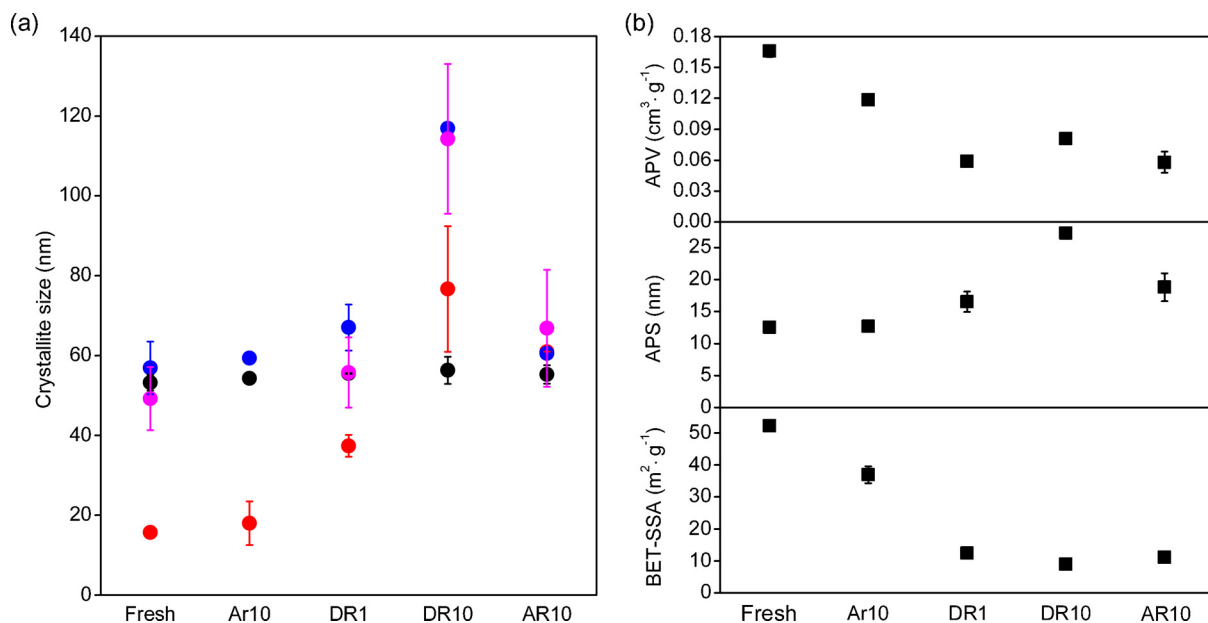
Fig. 4. (a) Crystallite size of m-ZrO_2 (●), t-ZrO_2 (●), FeO_X (●) and Ni_3Fe (●) phases in the fresh and spent samples (after 10 h Ar treatment at 750 °C and 10 bar (Ar10), 10 h dry reforming at 1 bar (DR1) or 10 bar (DR10), as well as 10 h auto-thermal dry reforming at 10 bar (AR10)) of the Fe/Zr@Zr-Ni@Zr bifunctional catalyst. Crystallite sizes and error bars were calculated based on XRD data (Fig. S6) by Gaussian fitting. Note that: FeO_X respectively represents the Fe_2O_3 phase in the fresh and Ar treated samples and the Fe_3O_4 phase in the samples after CH_4 reforming, the crystallite size of the Ni_3Fe phase in the fresh sample was obtained from the sample after reduction (at 750 °C and 1 bar); (b) BET specific surface area (BET-SSA), average pore size (APS) and average pore volume (APV) of the fresh and spent bifunctional catalysts. The error bars represent the standard deviation based on three repeat tests.
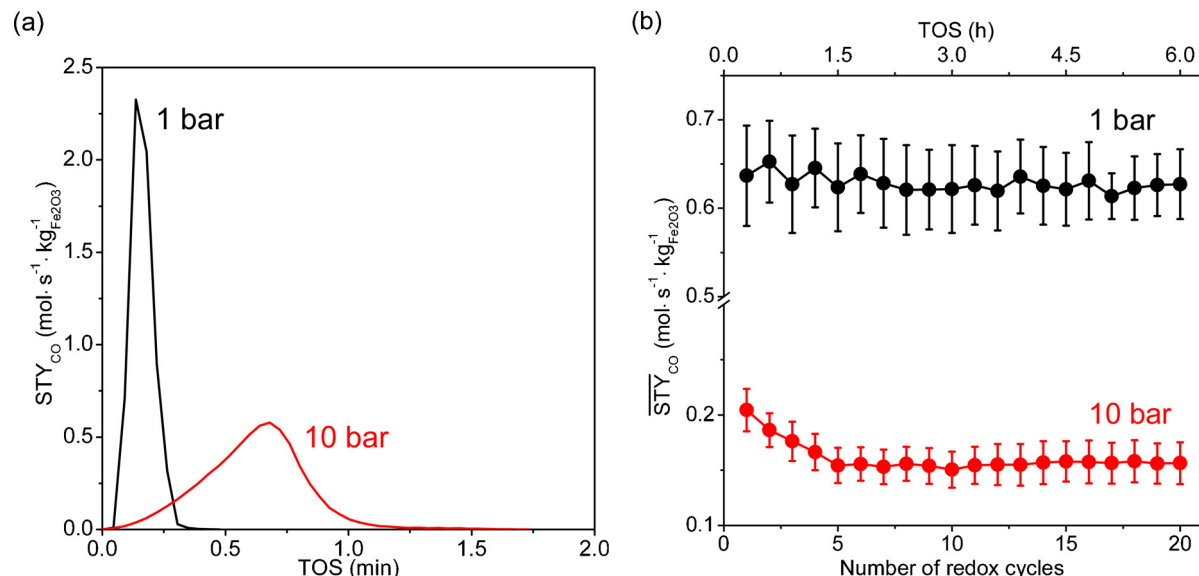

Fig. 5. (a) Space-time yield of CO (STY_{CO}, $mol·s^{-1}·kg_{Fe2O3}^{-1}$) vs. time-on-stream (TOS, min) in a H_2/CO_2 redox cycle over the Fe/Zr@Zr OSM at 750 °C, 1 bar and 10 bar pressure. A complete cycle (18 min) comprises 9 min of reduction half-cycle (4 min reduction followed by 5 min purging) and 9 min of re-oxidation half-cycle (4 min re-oxidation followed by 5 min purging). Reducing gas: 20% H_2/Ar; Re-oxidizing gas: 20% CO_2/Ar; Purging gas: pure Ar; Gas flow rates: 200 NmL·min^{-1}. (b) Time-averaged space-time yield ($\overline{STY}_{CO}$, $mol·s^{-1}·kg_{Fe2O3}^{-1}$) of CO in 4 min re-oxidation with 20% CO_2/Ar during 20 cycles of H_2/CO_2 redox cycling (totally 6 h time-on-stream) over the Fe/Zr@Zr OSM at 750 °C, 1 bar and 10 bar pressure. The bar represents the maximum and minimum of the oscillating CO space-time yield.

fully utilized for CO_2 reduction at the present experimental conditions.

The rise of pressure intensifies the non-ideal flow in the reactor, resulting in a longer gas residence time, thereby showing a broader STY_{CO} peak over TOS (Fig. 5a). The latter leads to a lower time-averaged space-time yield of CO, as seen in Fig. 5b, with the initial CO $\overline{STY}$ at 10 bar being over 3 times lower than that at 1 bar. Comparison of the CO $\overline{STY}$ in 20 redox cycles (totally 6 h) allows to evaluate the redox stability of the Fe/Zr@Zr OSM at different pressures. During 6 h of redox cycling at 1 bar, the CO production keeps stable with a constant $\overline{STY}$ of ~ 0.63 $mol·s^{-1}·kg_{Fe2O3}^{-1}$, while at 10 bar it rapidly declines from

0.2 to 0.15 $mol·s^{-1}·kg_{Fe2O3}^{-1}$ in the first 5 cycles, showing a fast deactivation of the OSM, before reaching a steady level (Fig. 5b).

Because the feed of 20% H_2/Ar generates no carbon during the reduction half-cycle in the H_2/CO_2 redox cycling, the deactivation of the Fe/Zr@Zr OSM can be attributed solely to sintering, as verified from the STEM-EDX mapping of the spent OSM (Fig. 6). Compared to the fresh sample (Fig. S1c), large clusters of OSM are observed in the spent samples, indicating the aggregation of particles during redox cycling. The increase in Fe particle size after redox cycling is clearly observed (in the EDX element mapping) for both 1 bar (labelled as spent_RC1)
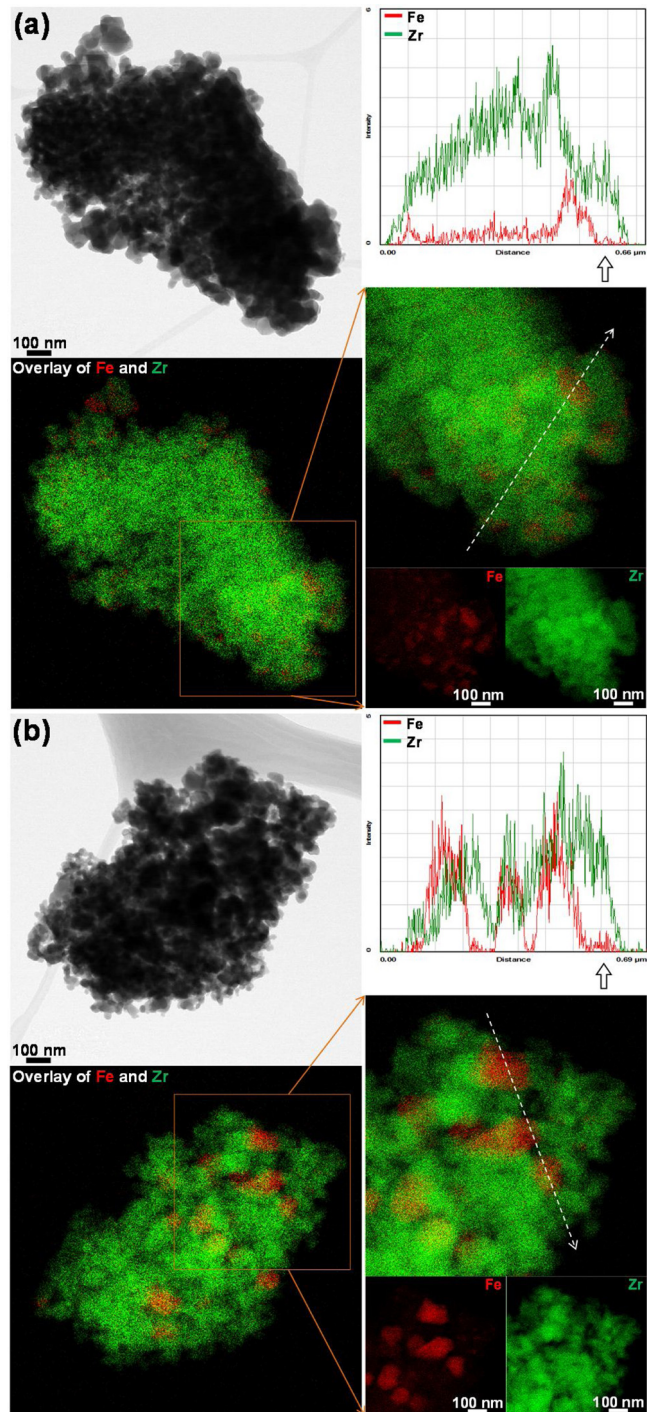
Fig. 6. STEM micrograph, EDX element mapping of Fe (red color), Zr (green) and their overlay mapping, as well as EDX line-scan analysis for the samples of Fe/Zr@Zr OSM after 20 cycles of H_2/CO_2 redox cycling at 750 °C and 1 bar (a) or 10 bar (b). The dashed white arrows on the zoomed in region of mappings show the X-ray scanning route through the particle.

and 10 bar (spent_RC10), while the Fe particle in the spent_RC10 is obviously larger than the one in the spent_RC1, indicating that Fe sintering is more severe at high-pressure redox cycling. This can be further evidenced from Fig. 7a, where the increase in crystallite size of iron oxide is presented after 20 cycles of redox cycling, which is more substantial for the spent_RC10. The increase in crystallite size of m-ZrO_2 and t-ZrO_2 is also confirmed, indicating the sintering of both core and shell, which will lead to the decay of the core-shell structure of the Fe/

Zr@Zr OSM, during prolonged redox cycling. However, as shown by the zoomed EDX mappings, the Fe particles are still uniformly encapsulated by Zr in the spent_RC1 (Fig. 6a), meaning that the core-shell structure of the OSM is preserved for redox cycling at atmospheric pressure. In the spent_RC10 (Fig. 6b), the Fe particles show a tendency to migrate out of the Zr shell, illustrating the damaging of the core-shell structure at high-pressure redox cycling. The latter is in line with the smaller specific surface area and the larger average pore size, i.e. a more important collapse of the mesopores, of the spent_RC10, compared to the spent_RC1 (Fig. 7b). In contrast, even after 10 h Ar treatment at 750 °C and 10 bar (Ar10), the spent sample only shows slight changes in both crystallite sizes (Fig. 7a) and texture properties (Fig. 7b), demonstrating that the OSM is not sensitive to sintering under pressurized operation in the absence of redox reactions, consistent with the influence of pressure on the behavior of the bifunctional catalyst found in §3.2.1.

Sintering, as a consequence of the crystallite growth of either the active phases or the support materials, is a physical process that is strongly temperature dependent. The so-called Tamman temperature ($T_{Tamman} = 0.5 T_{melting}$) is used as indicative for the temperature at which sintering may occur. From T_{Tamman} onwards, particles start showing mobility [58], allowing them to create larger aggregates. In H_2/CO_2 redox cycling, the sintering of the Fe/Zr@Zr OSM depends on the material's state during reaction. As determined by in-situ XRD (Fig. 1a), the OSM goes through three phases, i.e. $Fe_3O_4 \rightarrow FeO \rightarrow Fe$, during the reduction half-cycle. The $T_{melting}$ of Fe_3O_4, FeO and Fe phases are 1597, 1377, and 1538 °C, respectively. Thus, the formation of FeO as intermediate during the reduction process naturally decreases the melting point of the OSM. This will lead to faster material sintering, since the reaction temperature ($T_R = 750$ °C) is higher than the T_{Tamman} (= 688.5 °C) when the state of the OSM is FeO. The longer the OSM remains in FeO phase, the more serious its sintering will be. Fig. S8 illustrates in a schematic way the origin of the deactivation of the Fe/Zr@Zr OSM during H_2/CO_2 redox cycling. At 1 bar, the reduction of the OSM is very fast, only requiring ~20 s to transform Fe_3O_4 into metallic Fe. At 10 bar, however, the non-ideal gas flow slows down the transformation, so that complete reduction of Fe_3O_4 to Fe now takes up 55 s, almost 3 times as long. Hence, during the OSM reduction process, the rise of pressure prolongs the existence time of the FeO intermediate state, thereby increasing the time in which enhanced sintering can occur. As a result, the OSM will suffer more seriously from sintering at high-pressure redox cycling.

3.2.3. The behavior of the double-zone reactor bed

A double-zone reactor bed (Fig. S2c), constructed from an upper Fe/Zr@Zr-Ni@Zr bifunctional catalyst zone and a lower Fe/Zr@Zr OSM zone, was applied for the entire CCAR process. This comprises first a reduction half-cycle, i.e. auto-thermal dry reforming of CH_4 over the bifunctional catalyst, producing syngas and H_2O, and reduction of the OSM by the generated syngas, followed by the re-oxidation half-cycle, i.e. the regeneration of the OSM by CO_2 accompanied with CO production. The effect of pressure on the behavior of the double-zone bed was assessed over 20 cycles of CCAR at 750 °C, 1 bar and 10 bar. The total molar yield (mol·kg_{Ni}^{-1}) of each product component during the reduction half-cycle of CCAR (in the first cycle) is displayed in Table S2. Therefrom, the product composition (in molar percentage) in the reduction half-cycle at different pressures can be calculated to further analyze the influence of pressure on the activity of the double-zone bed, as shown in Fig. 8a.

O_2 gets completely converted at both pressures. Compared to 1 bar, the mole fractions of CH_4, CO_2, H_2O and C increase at 10 bar pressure, while the mole fractions of CO and H_2 decrease in the product. This translates into decreasing of CH_4 and CO_2 conversion, decrease of CO and H_2 production and increase of H_2O and deposited carbon, with the rise of pressure. These trends follow the variation of the equilibrium product composition with pressure predicted by the thermodynamic analysis (Fig. 8b). Even though carbon deposition is largely suppressed
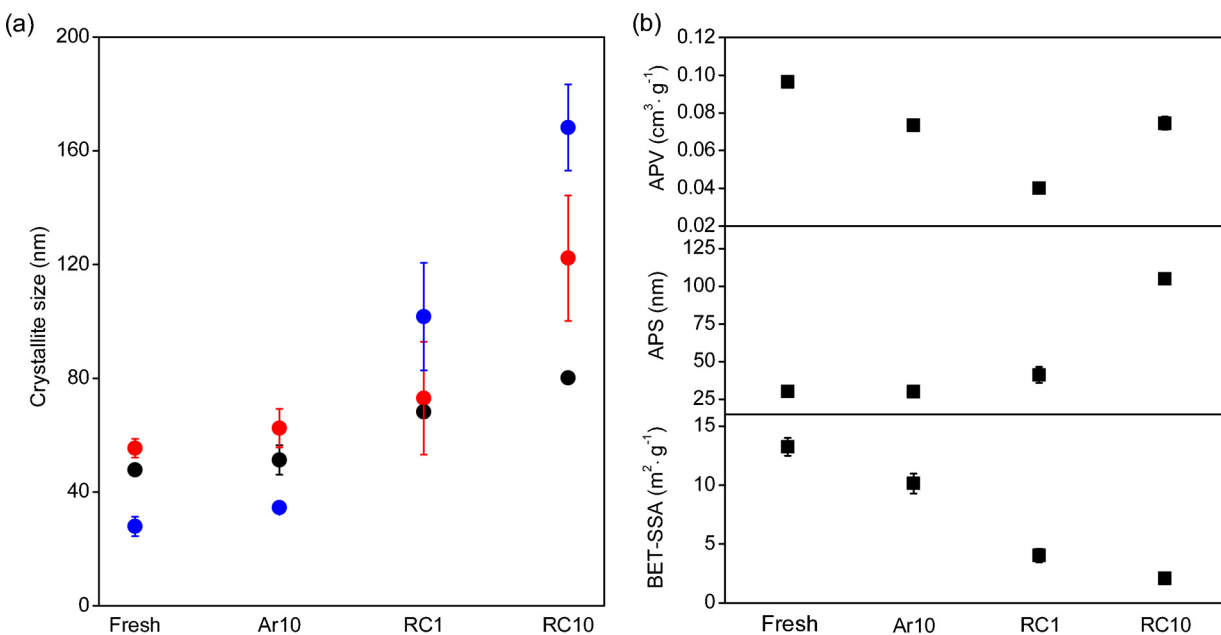
Fig. 7. (a) Crystallite size of m-ZrO$_2$ (●), t-ZrO$_2$ (●) and FeO$_X$ (●) phases in the fresh sample and the samples after 10 h Ar treatment at 750 °C and 10 bar (Ar10) and 20 redox cycles at 750 °C and 1 bar (RC1) or 10 bar (RC10) of the Fe/Zr@Zr OSM. Crystallite size and error bar were calculated based on XRD data (Fig. S7) by Gaussian fitting. Note that: FeO$_X$ respectively represents the Fe$_2$O$_3$ phase in the fresh and Ar treated samples and the Fe$_3$O$_4$ phase in the samples after redox cycles, because the redox cycling ends with the re-oxidation half-cycle, in which the oxidation degree of metallic Fe by CO$_2$ can maximally reach Fe$_3$O$_4$ state; (b) BET specific surface area (BET-SSA), average pore size (APS) and average pore volume (APV) of the fresh and spent OSMs. The error bars represent the standard deviation based on three repeat tests.

by the added O$_2$ during auto-thermal dry reforming of CH$_4$ (feed: CH$_4$:CO$_2$:O$_2$:Ar = 1:1:0.1:0.3), a small amount of carbon inevitably forms on the bifunctional catalyst during the reduction half-cycle of CCAR, involving the same feed gas, which has been confirmed in §3.2.1. However, the deposited carbon can be effectively removed by oxidation with CO$_2$ (CO$_2$ + C → 2CO) in the re-oxidation half-cycle of CCAR. For instance, during 1 bar CCAR, a higher CO molar yield (46.8 mol·kg$_{Fe2O3}$$^{-1}$), compared to the theoretical yield value (~ 17 mol·kg$_{Fe2O3}$$^{-1}$), is obtained during the re-oxidation half-cycle, indicating a considerable production of CO by carbon oxidation with CO$_2$. The removal of the deposited carbon with CO$_2$ in the re-oxidation half-cycle of catalyst-assisted chemical looping was equally reported in previous studies [28,39,59].

The stability of the double-zone reactor bed during CCAR can be monitored via the changes in the CH$_4$ conversion in the reduction half-cycle and the CO STY in the re-oxidation half-cycle over 20 cycles (Fig. 9). Similar to the conclusion obtained from Fig. 2 in §3.2.1, the initial CH$_4$ conversion (in the 1st cycle) at 1 bar (90%) is higher than the one at 10 bar (64%) during the reduction half-cycle of CCAR (Fig. 9a). Both values are decreased after 20 cycles, but the latter declines (by 48%) more than the former (by 18%). This indicates that the elevation of pressure not only reduces the initial catalytic activity, but also aggravates the deactivation of the double-zone bed for auto-thermal dry reforming of CH$_4$. Owing to the advantage of CCAR in the elimination of carbon deposition, the loss of catalytic activity should now mainly be attributed to the sintering of Ni particles in the Fe/Zr@
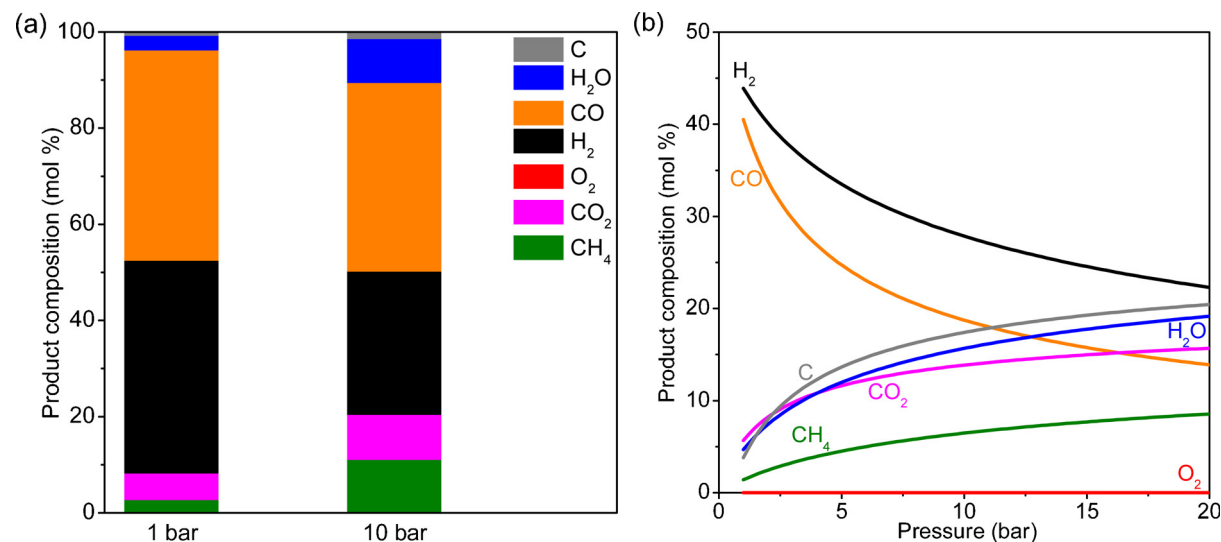

Fig. 8. (a) The experimental product composition during the reduction half-cycle of CCAR at 750 °C and 1 bar or 10 bar, based on the data in Table S2; (b) Equilibrium product composition as a function of pressure during the reforming of a mixture of CH$_4$:CO$_2$:O$_2$:Ar = 1:1:0.1:0.3 at 750 °C.
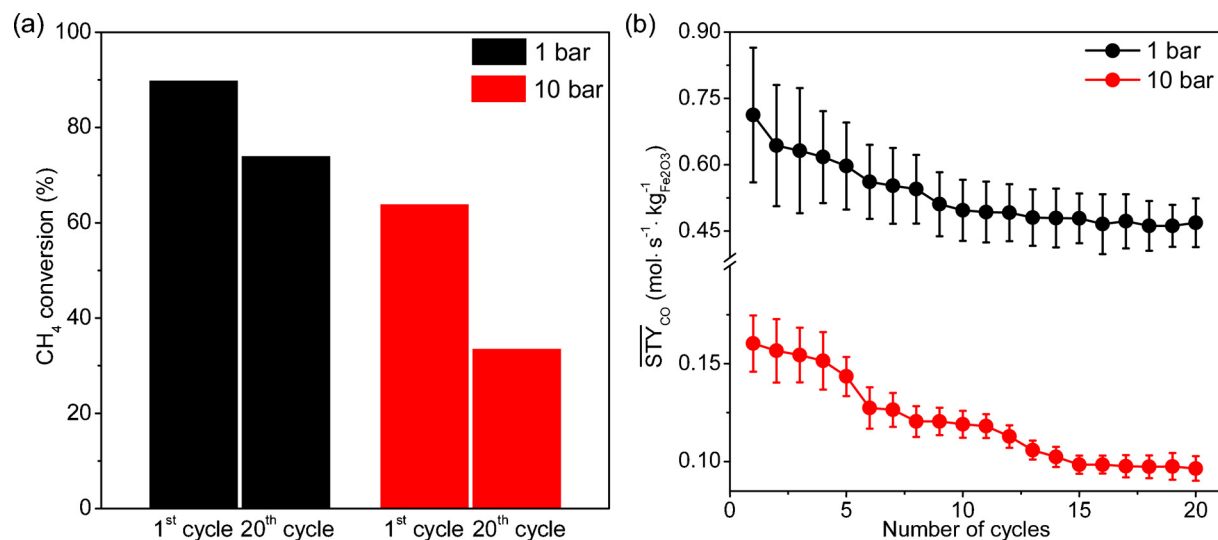
Fig. 9. (a) CH$_4$ conversion in the reduction half-cycle of the 1st and 20th cycle of the prolonged CCAR as well as (b) $\overline{STY}$ of CO in the re-oxidation half-cycle during 20 cycles of CCAR at 1 bar and 10 bar over the double-zone reactor bed. The bar represents the maximum and minimum of the oscillating CO space-time yield. A complete cycle (18 min) comprises 9 min of reduction half-cycle (2 min reduction followed by 7 min purging) and 9 min of re-oxidation half-cycle (2 min re-oxidation followed by 7 min purging). Reducing gas: mixture of CH$_4$:CO$_2$:O$_2$:Ar = 1:1:0.1:0.3; Re-oxidizing gas: 20% CO$_2$/Ar; Purging gas: pure Ar; Gas flow rates: 200 NmL·min^{-1}.
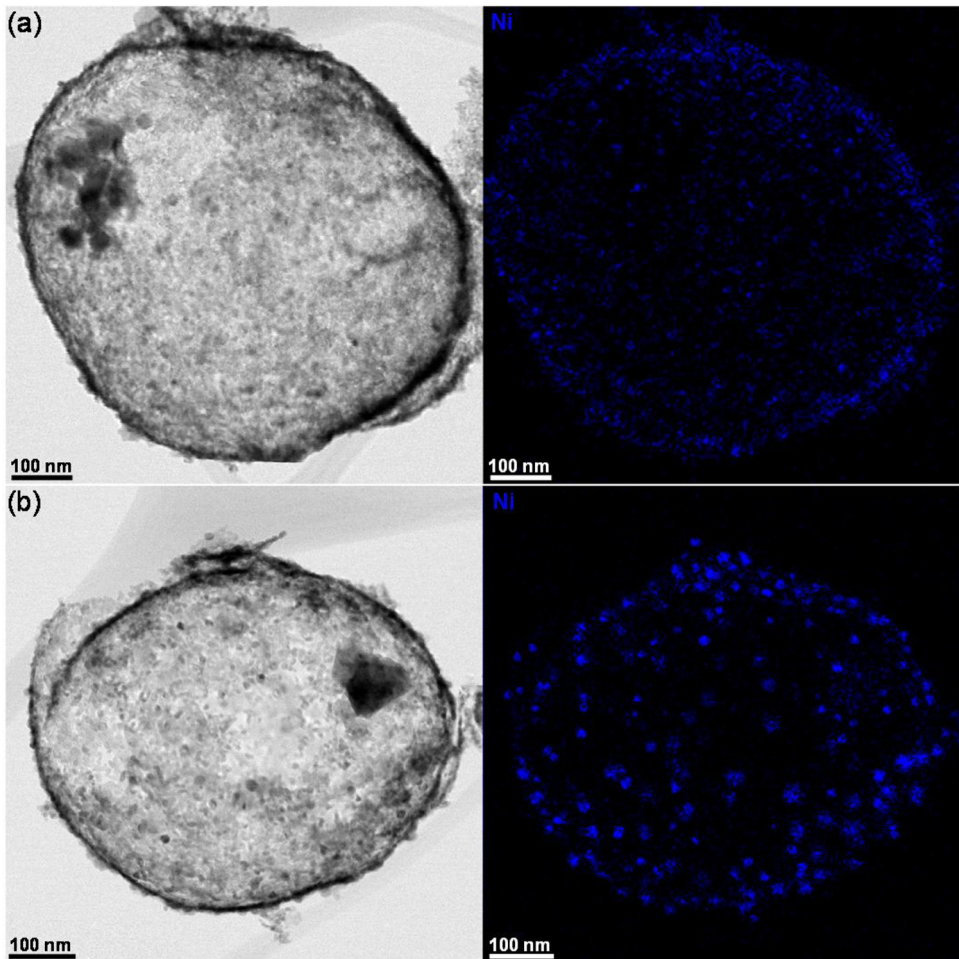

Fig. 10. STEM micrograph and EDX element mapping of Ni for the samples of the Fe/Zr@Zr-Ni@Zr bifunctional catalyst from the double-zone reactor bed after 20 cycles of CCAR at 1 bar (a) and 10 bar (b).

Zr-Ni@Zr bifunctional catalyst. The latter can be confirmed by STEM imaging and EDX element mapping of Ni, as seen in Fig. 10.

The spent catalysts do retain their core-shell structure after 20 cycles of CCAR, and carbon filaments are not observed on the catalyst surface. However, an increase in particle size of Ni (compared to the fresh catalyst shown in Fig. S1g) is seen in the spent catalysts, evidencing Ni sintering, and the sintered Ni particles in the spent sample from 10 bar CCAR are clearly larger than the ones from 1 bar CCAR. In addition, comparison of the Ni particle size in the catalyst after CH_4 auto-thermal dry reforming (Fig. 3c) and the one after CCAR cycling (Fig. 10b) at 10 bar pressure, shows that the latter is much smaller than the former, further confirming the advantage of the CCAR process for maintaining the stability of the catalyst (due to the elimination of deposited carbon by CO_2 during the re-oxidation half-cycle) over the conventional auto-thermal dry reforming process at high pressure.

As shown in Fig. 9b, the initial STY of CO at 10 bar (0.16 $mol \cdot s^{-1} \cdot kg_{Fe2O3}^{-1}$) is over 4 times lower than that at 1 bar (0.71 $mol \cdot s^{-1} \cdot kg_{Fe2O3}^{-1}$) during the re-oxidation half-cycle of CCAR, in line with the trend illustrated by Fig. 5b in §3.2.2. Both CO yields decline continuously over the repeated cycles. The CO STY at 1 bar drops slowly, almost reaching a stable level after 10 cycles (30% loss of initial value). The CO STY at 10 bar, however, drops throughout the 20 cycles (40% loss). These results indicate that the rise of pressure not only decreases the initial time-averaged space-time yield of CO from CO_2 reduction, but also promotes the deactivation of the double-zone bed for CO_2 utilization.

Next to sintering of Ni, also Fe particles increase in size, an additional factor in weakening the reactivity of the double-zone bed for CO_2 utilization. Fig. 11a shows the increase in crystallite size of iron oxides in both bifunctional catalyst and OSM after 20 cycles of CCAR, where the sintering of iron oxide in the OSM appears more sensitive to the rise of pressure than in the bifunctional catalyst. This is confirmed by the EDX element mapping of Fe for the spent materials after 10 bar CCAR cycling (Fig. S9). The lesser degree of sintering of Fe particles in the bifunctional catalyst can be attributed to the prevention of Fe particles aggregation by the two layers of ZrO_2 coating, one from the Fe/Zr@Zr core and the other from the Ni@Zr shell, as well as the higher stability of this ZrO_2 shell, indicated by the unchanged crystallite size of t-ZrO_2 (the crystal phase of ZrO_2 shell) after 20 cycles of CCAR (Fig. 11b). According to the conclusion obtained from Fig. 1 in §3.1, the OSM in the second zone is considered to provide the main oxygen storage capacity of the double-zone reactor bed for CO_2 conversion during the re-oxidation half-cycle. Hence, a more severe sintering of the OSM at elevated pressure means a larger loss in the ability of the double-zone reactor bed to utilize CO_2, corresponding to the more significant decline in CO STY at 10 bar CCAR cycling.

Furthermore, from comparison of the CO production between H_2/CO_2 redox cycling (Fig. 5b) and CCAR cycling (Fig. 9b), the latter shows a larger decline after 20 cycles (same total duration) at both 1 bar and 10 bar, implying that sintering of the OSM is not the only reason for this deactivation. In general, the conversion of CO_2 upon OSM re-oxidation
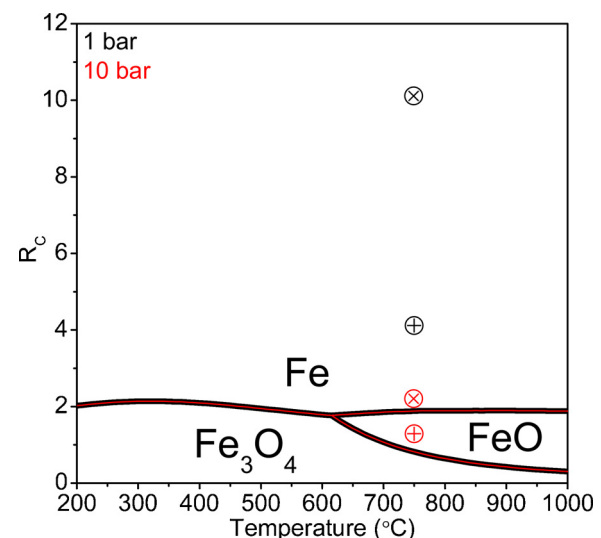

Fig. 12. Thermodynamic analysis of the reduction degree of the OSM as a function of the reduction capacity (R_C) of the product gas mixture in the reduction half-cycle of CCAR (feed: CH_4:CO_2:O_2:Ar = 1:1:0.1:0.3): the equilibrium R_C lines of the phase transformation of the iron/iron oxide system at different temperatures and pressures (1 bar: black, 10 bar: red). The circles "$\otimes$" and "$\oplus$" respectively indicate the experimental value of the R_C in the 1st cycle and 20th cycle of CCAR (at 750 °C, 1 bar (black) and 10 bar (red)).

strongly depends on the achieved reduction degree of the OSM, determining the amount of oxygen vacancies. As revealed by thermodynamics (Fig. 12), the transformation from Fe_3O_4 to metallic Fe highly depends on the reduction capacity (R_C) of the gas products in the reduction half-cycle. R_C is defined as the ratio between reducing and oxidizing gases, i.e. (H_2 + CO)/(H_2O + CO_2). The co-fed O_2 is here not considered because it is totally consumed. For reaction at 750 °C, Fe_3O_4 can be reduced to FeO as R_C increases to > 0.8, and metallic Fe is reached when R_C is higher than 1.9. During the reduction half-cycle of CCAR, the R_C of the product gases is highly controlled by the CH_4 and CO_2 conversions: high conversion entails high R_C values, for relatively low conversions, R_C equally remains low, resulting in an inadequate reduction of the OSM [39]. Compared to the R_C values in the first cycle, after 20 cycles of CCAR, R_C decreases to considerably lower values, especially at 10 bar experiment, the R_C has dropped to the FeO region, obviously indicating a low reduction degree of the OSM. In this sense, along with the repeated cycles, the decrease of the CH_4 and CO_2 conversions results in a gradually lower reduction capacity of the product mixture during the reduction half-cycle, thereby leading to a decrease of the achievable reduction degree of the OSM. Eventually, the CO yield, derived from the OSM regeneration with CO_2 in the re-oxidation half-cycle, declines. Therefore, the deactivation of the bifunctional catalyst is another factor in weakening the CO_2 utilization capacity of
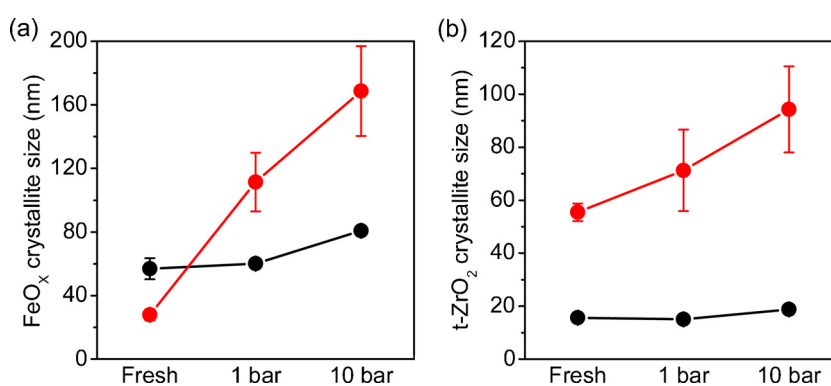

Fig. 11. Crystallite size of FeO_X (a) and t-ZrO_2 (b) phases in fresh and spent samples (after 20 cycles of CCAR at 1 bar and 10 bar) of the Fe/Zr@Zr-Ni@Zr bifunctional catalyst (●) or Fe/Zr@Zr OSM (•) from the double-zone reactor bed. Crystallite size and error bar were calculated based on XRD data (Fig. S10) by Gaussian fitting. Note that: FeO_X respectively represents the Fe_2O_3 phase of the fresh sample and the Fe_3O_4 phase of the spent samples, because the CCAR cycling ends with the re-oxidation half-cycle, in which oxidation of metallic Fe by CO_2 can at most reach the Fe_3O_4 state.

the double-zone bed. Overall, the stability of the double-zone reactor bed for CO_2 utilization in successive CCAR cycles is controlled by the stability of the first-zone Fe/Zr@Zr-Ni@Zr bifunctional catalyst and the second-zone Fe/Zr@Zr oxygen storage material and deactivation of both materials will decrease the total oxygen storage capacity that can used for CO_2 reduction to CO.

4. Conclusions

A Fe/Zr@Zr-Ni@Zr bifunctional nanomaterial with an eccentric core-shell structure was combined with a core-shell Fe/Zr@Zr oxygen storage material in a double-zone reactor bed for catalyst-assisted chemical looping. The bifunctional catalyst provides two functions, catalyst (for CH_4 dry reforming) and oxygen storage material (for CO_2 cyclic utilization), by its shell and core, respectively. To overcome its limited oxygen storage capacity, supplementary Fe/Zr@Zr oxygen storage material was provided in the second zone. This double-zone reactor bed configuration was tested for catalyst-assisted chemical looping CH_4 dry reforming (CCDR) and catalyst-assisted auto-thermal chemical looping (CCAR) at 1 bar and 10 bar.

The effect of pressure on the catalytic performance of the Fe/Zr@Zr-Ni@Zr bifunctional catalyst was firstly investigated by steady-state CH_4 dry or auto-thermal dry reforming (i.e. without or with O_2 in the feed) at 750 °C and 1 or 10 bar. The increase of pressure not only decreases the initial CH_4 conversion, but also favours carbon formation, accordingly aggravating the deactivation of Fe/Zr@Zr-Ni@Zr. The latter can be effectively mitigated by co-feeding a small amount of O_2 with CH_4 and CO_2. The origin of the pressure-induced deactivation of Fe/Zr@Zr-Ni@Zr is reaction-related: when dry reforming reaction occurs on the catalyst, high pressure promotes the deposition of carbon on the Ni surface, the deposited carbon proliferates and forms carbon filaments, which encapsulate the Ni-based particles and push them outward, resulting in the collapse of the core-shell structure and concomitant more severe particle sintering.

The redox properties of the Fe/Zr@Zr oxygen storage material were evaluated over 20 cycles of H_2/CO_2 redox cycling at 750 °C and 1 or 10 bar. While in the initial stage, the oxygen storage capacity of Fe/Zr@Zr can be fully utilized for CO_2 reduction, the rise of pressure decreases the time-averaged space-time yield of CO. This pressure-induced deactivation of Fe/Zr@Zr during redox cycling is also reaction-related, its origin being the fast sintering during the phase transformation of the oxygen storage material in the reduction step. The formation of a FeO intermediate phase decreases the melting point of the material, weakening its tolerance to sintering. High pressure prolongs the presence of the FeO state, which thus leads to more serious sintering.

Finally, the effect of pressure on the performance of the double-zone reactor bed was investigated over 20 cycles of CCAR process at 750 °C. The influence of increasing pressure on the activity and stability of the double-zone bed is in line with the observations as mentioned above. Although the CCAR process has an advantage in the elimination of carbon, deactivation of the double-zone reactor bed was still present, which is mainly ascribed to the particle sintering. The loss in ability for CO_2 utilization depends on both deactivation of the bifunctional catalyst in the first zone and the oxygen storage material in the second zone. Even though the latter controls the dominant oxygen storage capacity for CO_2 reduction to CO during the re-oxidation half-cycle, the former determines the reduction capacity of the produced gas in the reduction half-cycle, thereby affecting the achievable reduction degree of Fe_3O_4, which in turn influences the achievable CO_2 conversion upon the re-generation of the oxygen storage material.

Acknowledgements

Appendix A. Supplementary data

Supplementary material related to this article can be found, in the online version, at doi:https://doi.org/10.1016/j.apcatb.2019.01.084.

References

[1] M. Tang, L. Xu, M. Fan, Progress in oxygen carrier development of methane-based chemical-looping reforming: a review, Appl. Energy 151 (2015) 143–156.

[2] J. Adanez, A. Abad, F. Garcia-Labiano, P. Gayan, L.F.D. Diego, Progress in chemical-looping combustion and reforming technologies, Prog. Energy Combust. Sci. 38 (2012) 215–282.

[3] B. Li, Y. Duan, D. Luebke, B. Morreale, Advances in CO_2 capture technology: a patent review, Appl. Energy 102 (2013) 1439–1447.

[4] A. Das, D.M. D'Alessandro, V.K. Peterson, Carbon dioxide separation, capture, and storage in porous materials, in: G. Kearley, V. Peterson (Eds.), Neutron Applications in Materials for Energy. Neutron Scattering Applications and Techniques, Springer, Cham, 2015, pp. 33–60.

[5] L. Guo, J. Yang, G. Hu, X. Hu, H. DaCosta, M. Fan, CO_2 removal from flue gas with amine-impregnated titanate nanotubes, Nano Energy 25 (2016) 1–8.

[6] M.K. Mondal, H.K. Balsora, P. Varshney, Progress and trends in CO_2 capture/separation technologies: a review, Energy 46 (2012) 431–441.

[7] S.D. Kenarsari, D. Yang, G. Jiang, S. Zhang, J. Wang, A.G. Russell, Q. Wei, M. Fan, Review of recent advances in carbon dioxide separation and capture, RSC Adv. 3 (2013) 22739–22773.

[8] E. Zedillo, Global Warming: Looking Beyond Kyoto, Pentagon Press, 2008.

[9] X. Chen, J. Jiang, K. Li, S. Tian, F. Yan, Energy-efficient biogas reforming process to produce syngas: the enhanced methane conversion by O_2, Appl. Energy 185 (2017) 687–697.

[10] J.A. Martens, A. Bogaerts, N.D. Kimpe, P.A. Jacobs, G.B. Marin, K. Rabaey, M. Saeys, S. Verhelst, The chemical route to a carbon dioxide neutral world, ChemSusChem 10 (2017) 1039–1055.

[11] M. Najera, R. Solunke, T. Gardner, G. Veser, Carbon capture and utilization via chemical looping dry reforming, Chem. Eng. Res. Des. 89 (2011) 1533–1543.

[12] S. Bhavsar, M. Najera, G. Veser, Chemical looping dry reforming as novel, intensified process for CO_2 activation, Chem. Eng. Technol. 35 (2012) 1281–1290.

[13] L.-S. Fan, L. Zeng, S. Luo, Chemical-looping technology platform, AIChE J. 61 (2015) 2–22.

[14] Z. Huang, H. Jiang, F. He, D. Chen, G. Wei, K. Zhao, A. Zheng, Y. Feng, Z. Zhao, H. Li, Evaluation of multi-cycle performance of chemical looping dry reforming using CO_2 as an oxidant with Fe–Ni bimetallic oxides, J. Energy Chem. 25 (2016) 62–70.

[15] A. Löfberg, T. Kane, J. Guerrero-Caballero, L. Jalowiecki-Duhamel, Chemical looping dry reforming of methane: toward shale-gas and biogas valorization, Chem. Eng. Process.: Process Intensif. 122 (2017) 523–529.

[16] M. Kathe, A. Empfield, P. Sandvik, C. Fryer, Y. Zhang, E. Blair, L.-S. Fan, Utilization of CO_2 as a partial substitute for methane feedstock in chemical looping methane-steam redox processes for syngas production, Energy Environ. Sci. 10 (2017) 1345–1349.

[17] V.V. Galvita, H. Poelman, C. Detavernier, G.B. Marin, Catalyst-assisted chemical looping for CO_2 conversion to CO, Appl. Catal. B 164 (2015) 184–191.

[18] M.D. Symes, L. Cronin, Decoupling hydrogen and oxygen evolution during electrolytic water splitting using an electron-coupled-proton buffer, Nat. Chem. 5 (2013) 403.

[19] D. Voiry, H. Yamaguchi, J. Li, R. Silva, D.C.B. Alves, T. Fujita, M. Chen, T. Asefa, V.B. Shenoy, G. Eda, M. Chhowalla, Enhanced catalytic activity in strained chemically exfoliated WS2 nanosheets for hydrogen evolution, Nat. Mater. 12 (2013) 850.

[20] Y. Cao, Z. Gao, J. Jin, H. Zhou, M. Cohron, H. Zhao, H. Liu, W. Pan, Synthesis gas production with an adjustable H_2/CO ratio through the coal gasification process: effects of coal ranks and methane addition, Energy Fuels 22 (2008) 1720–1730.

[21] Y. Liu, D. Yuan, D. Ji, Z. Li, Z. Zhang, B. Wang, H. Wu, Syngas production: diverse H_2/CO range by regulating carbonates electrolyte composition from CO_2/H_2O via co-electrolysis in eutectic molten salts, RSC Adv. 7 (2017) 52414–52422.

[22] K. Verbeeck, L.C. Buelens, V.V. Galvita, G.B. Marin, K.M. Van Geem, K. Rabaey, Upgrading the value of anaerobic digestion via chemical production from grid injected biomethane, Energy Environ. Sci. 11 (2018) 1788–1802.

[23] L.C. Buelens, V.V. Galvita, H. Poelman, C. Detavernier, G.B. Marin, Super-dry reforming of methane intensifies CO_2 utilization via Le Chatelier's principle, Science 354 (2016) 449–452.

[24] V.V. Galvita, H. Poelman, G.B. Marin, Hydrogen production from methane and carbon dioxide by catalyst-assisted chemical looping, Top. Catal. 54 (2011) 907–913.

[25] B. Christian Enger, R. Lødeng, A. Holmen, A review of catalytic partial oxidation of methane to synthesis gas with emphasis on reaction mechanisms over transition metal catalysts, Appl. Catal. A Gen. 346 (2008) 1–27.

[26] W.-H. Chen, S.-C. Lin, Characterization of catalytic partial oxidation of methane with carbon dioxide utilization and excess enthalpy recovery, Appl. Energy 162 (2016) 1141–1152.

[27] M.P. Kohn, M.J. Castaldi, R.J. Farrauto, Auto-thermal and dry reforming of landfill

gas over a Rh/γ-Al₂O₃ monolith catalyst, Appl. Catal. B 94 (2010) 125–133.

[28] J. Hu, L. Buelens, S.-A. Theofanidis, V.V. Galvita, H. Poelman, G.B. Marin, CO₂ conversion to CO by auto-thermal catalyst-assisted chemical looping, J. CO₂ Util. 16 (2016) 8–16.

[29] J. Hu, V.V. Galvita, H. Poelman, G.B. Marin, Advanced chemical looping materials for CO₂ utilization: a Review, Materials 11 (2018) 1187.

[30] L. Zeng, Z. Cheng, J.A. Fan, L.-S. Fan, J. Gong, Metal oxide redox chemistry for chemical looping processes, Int. Rev. Chem. Eng. 2 (2018) 349.

[31] N.V.R.A. Dharanipragada, L.C. Buelens, H. Poelman, E. De Grave, V.V. Galvita, G.B. Marin, Mg–Fe–Al–O for advanced CO₂ to CO conversion: carbon monoxide yield vs. Oxygen storage capacity, J. Mater. Chem. A 3 (2015) 16251–16262.

[32] D. Zeng, Y. Qiu, S. Peng, C. Chen, J. Zeng, S. Zhang, R. Xiao, Enhanced hydrogen production performance through controllable redox exsolution within CoFeAlOₓ spinel oxygen carrier materials, J. Mater. Chem. A 6 (2018) 11306–11316.

[33] F. He, X. Li, K. Zhao, Z. Huang, G. Wei, H. Li, The use of La₁₋ₓSrₓFeO₃ perovskite-type oxides as oxygen carriers in chemical-looping reforming of methane, Fuel 108 (2013) 465–473.

[34] B. Bulfin, J. Vieten, D.E. Starr, A. Azarpira, C. Zachäus, M. Hävecker, K. Skorupska, M. Schmücker, M. Roeb, C. Sattler, Redox chemistry of CaMnO₃ and Ca₀.₈Sr₀.₂MnO₃ oxygen storage perovskites, J. Mater. Chem. A 5 (2017) 7912–7919.

[35] J. Han, S. Lu, C. Jin, M. Wang, R. Guo, Fe₃O₄/PANI/m-SiO₂ as robust reactive catalyst supports for noble metal nanoparticles with improved stability and re-cyclability, J. Mater. Chem. A 2 (2014) 13016–13023.

[36] A. Shafiefarhood, N. Galinsky, Y. Huang, Y. Chen, F. Li, Fe₂O₃@LaₓSr₁₋ₓFeO₃ core-shell redox catalyst for methane partial oxidation, ChemCatChem 6 (2014) 790–799.

[37] J. Hu, V.V. Galvita, H. Poelman, C. Detavernier, G.B. Marin, A core-shell structured Fe₂O₃/ZrO₂@ZrO₂ nanomaterial with enhanced redox activity and stability for CO₂ conversion, J. CO₂ Util. 17 (2017) 20–31.

[38] J. Zhang, F. Li, Coke-resistant Ni@SiO₂ catalyst for dry reforming of methane, Appl. Catal. B 176–177 (2015) 513–521.

[39] J. Hu, V.V. Galvita, H. Poelman, C. Detavernier, G.B. Marin, Catalyst-assisted chemical looping auto-thermal dry reforming: spatial structuring effects on process efficiency, Appl. Catal. 231 (2018) 123–136.

[40] M.E. Dry, The Fischer–tropsch process: 1950–2000, Catal. Today 71 (2002) 227–241.

[41] O. Nordness, L. Han, Z. Zhou, G.M. Bollas, High-pressure chemical-looping of methane and synthesis gas with Ni and Cu oxygen carriers, Energy Fuels 30 (2015) 504–514.

[42] V. Spallina, B. Marinello, F. Gallucci, M.C. Romano, M. Van Sint Annaland, Chemical looping reforming in packed-bed reactors: Modelling, experimental validation and large-scale reactor design, Fuel Process. Technol. 156 (2017) 156–170.

[43] R.Y. Chein, Y.C. Chen, C.T. Yu, J.N. Chung, Thermodynamic analysis of dry reforming of CH₄ with CO₂ at high pressures, J. Nat. Gas Sci. Eng. 26 (2015) 617–629.

[44] S.A. Theofanidis, V.V. Galvita, H. Poelman, N.V.R.A. Dharanipragada, A. Longo, M. Meledina, G. Van Tendeloo, C. Detavernier, G.B. Marin, Fe-containing magnesium aluminate support for stability and carbon control during methane reforming, ACS Catal. 8 (2018) 5983–5995.

[45] M. Usman, W.M.A. Wan Daud, H.F. Abbas, Dry reforming of methane: influence of process parameters—a review, Renew. Sustain. Energy Rev. 45 (2015) 710–744.

[46] J. Ni, L. Chen, J. Lin, S. Kawi, Carbon deposition on borated alumina supported nano-sized Ni catalysts for dry reforming of CH₄, Nano Energy 1 (2012) 674–686.

[47] K. Tomishige, Y. Himeno, Y. Matsuo, Y. Yoshinaga, K. Fujimoto, Catalytic performance and carbon deposition behavior of a NiO−MgO solid solution in methane reforming with carbon dioxide under pressurized conditions, Ind. Eng. Chem. Res. 39 (2000) 1891–1897.

[48] S. Takenaka, H. Ogihara, K. Otsuka, Structural change of Ni species in Ni/SiO₂ catalyst during decomposition of methane, J. Catal. 208 (2002) 54–63.

[49] K. Otsuka, H. Ogihara, S. Takenaka, Decomposition of methane over Ni catalysts supported on carbon fibers formed from different hydrocarbons, Carbon 41 (2003) 223–233.

[50] F. García-Labiano, J. Adánez, L.Fd. Diego, P. Gayán, A. Abad, Effect of pressure on the behavior of copper-, iron-, and nickel-based oxygen carriers for chemical-looping combustion, Energy Fuels 20 (2006) 26–33.

[51] H.P. Hamers, F. Gallucci, G. Williams, P.D. Cobden, M. van Sint Annaland, Reactivity of oxygen carriers for chemical-looping combustion in packed bed reactors under pressurized conditions, Energy Fuels 29 (2015) 2656–2663.

[52] I. Chorkendorff, J.W. Niemantsverdriet, Concepts of Modern Catalysis and Kinetics, Wiley, Hoboken, NJ, USA, 2006.

[53] B. Nolang, Ekvicalc and Ekvibase: Version 4.30; Svensk Energi Data, Balinge, Sweden (2013).

[54] W.L. Luyben, Design and control of the dry methane reforming process, Ind. Eng. Chem. Res. 53 (2014) 14423–14512.

[55] J.M. Ginsburg, J. Pina, T.E. Solh, H.Id. Lasa, Coke Formation over a nickel catalyst under methane dry reforming conditions: thermodynamic and kinetic models, Ind. Eng. Chem. Res. 44 (2005) 4846–4854.

[56] S.A. Theofanidis, V.V. Galvita, H. Poelman, G.B. Marin, Enhanced carbon-resistant dry reforming Fe-Ni catalyst: role of Fe, ACS Catal. 5 (2015) 3028–3039.

[57] S.A. Theofanidis, V.V. Galvita, H. Poelman, R. Batchu, L.C. Buelens, C. Detavernier, G.B. Marin, Mechanism of carbon deposits removal from supported Ni catalysts, Appl. Catal. B 239 (2018) 502–512.

[58] N.V.R.A. Dharanipragada, M. Meledina, V.V. Galvita, H. Poelman, S. Turner, G. Van Tendeloo, C. Detavernier, G.B. Marin, Deactivation study of Fe₂O₃–CeO₂ during redox cycles for CO production from CO₂, Ind. Eng. Chem. Res. 55 (2016) 5911–5922.

[59] N.V.R.A. Dharanipragada, V.V. Galvita, H. Poelman, L.C. Buelens, C. Detavernier, G.B. Marin, Bifunctional Co- and Ni- ferrites for catalyst-assisted chemical looping with alcohols, Appl. Catal. B 222 (2018) 59–72.